

# FINITE ELEMENT ANALYSIS OF DYNAMIC COMPACTION OF A STACK OF FOUR B-25 BOXES (U)

By

**CHUNG GONG**

**AUGUST 2001**

**UNCLASSIFIED**

DOES NOT CONTAIN  
UNCLASSIFIED CONTROLLED  
NUCLEAR INFORMATION

ADC &  
Reviewing  
Official:

*Cynthia P. Holding-Smith*  
(Cynthia P. Holding-Smith, Manager)

Date:

*9/15/2001*

## Patent Status

This internal management report is being transmitted without DOE patent clearance and no further dissemination or publication shall be made of the report without prior approval of the DOE-SR patent council.



---

**Westinghouse Savannah River Company  
Savannah River Technology Center  
Aiken, SC 29808**

Prepared for the U. S. Department of Energy under Contract DE-AC09-96SR18500

**This document was prepared in conjunction with work accomplished under Contract No. DE-AC09-96SR18500 with the U. S. Department of Energy.**

#### **DISCLAIMER**

**This report was prepared as an account of work sponsored by an agency of the United States Government. Neither the United States Government nor any agency thereof, nor any of their employees, makes any warranty, express or implied, or assumes any legal liability or responsibility for the accuracy, completeness, or usefulness of any information, apparatus, product or process disclosed, or represents that its use would not infringe privately owned rights. Reference herein to any specific commercial product, process or service by trade name, trademark, manufacturer, or otherwise does not necessarily constitute or imply its endorsement, recommendation, or favoring by the United States Government or any agency thereof. The views and opinions of authors expressed herein do not necessarily state or reflect those of the United States Government or any agency thereof.**

**This report has been reproduced directly from the best available copy.**

**Available for sale to the public, in paper, from: U.S. Department of Commerce, National Technical Information Service, 5285 Port Royal Road, Springfield, VA 22161,  
phone: (800) 553-6847,  
fax: (703) 605-6900  
email: [orders@ntis.fedworld.gov](mailto:orders@ntis.fedworld.gov)  
online ordering: <http://www.ntis.gov/support/index.html>**

**Available electronically at <http://www.doe.gov/bridge>  
Available for a processing fee to U.S. Department of Energy and its contractors, in paper, from: U.S. Department of Energy, Office of Scientific and Technical Information, P.O. Box 62, Oak Ridge, TN 37831-0062,  
phone: (865)576-8401,  
fax: (865)576-5728  
email: [reports@adonis.osti.gov](mailto:reports@adonis.osti.gov)**

**WSRC-TR-2001-00320**

**KEY WORDS:**

**Dynamic Compaction Analysis**

**Low Level Waste**

**B-25 Boxes**

**Engineered Trench**

**Soil Dynamics**

**Finite Element Analysis**

**Non-linear Elasto-plasticity**

**RETENTION PERIOD:**

**LIFETIME**

**FINITE ELEMENT ANALYSIS OF DYNAMIC COMPACTION OF  
A STACK OF FOUR B-25 BOXES (U)**

**By**

**CHUNG GONG**

**ISSUED: AUGUST 2001**

**SRTC**

**SAVANNAH RIVER TECHNOLOGY CENTER  
WESTINGHOUSE SAVANNAH RIVER COMPANY  
AIKEN, SC, 29808**

**Prepared for the U. S. Department of Energy under Contract DE-AC09-96SR18500**



**DOCUMENT:**

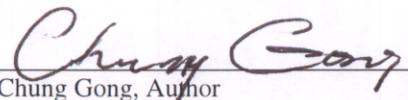
**WSRC-TR-2001-00320**

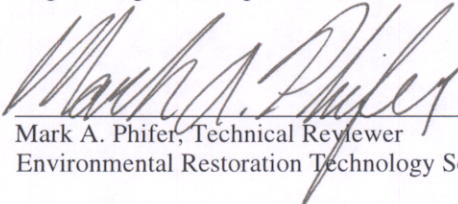
**TITLE:**

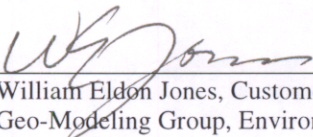
**FINITE ELEMENT ANALYSIS OF DYNAMIC COMPACTION OF A  
STACK OF FOUR B-25 BOXES (U)**

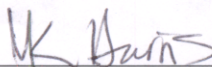
**APPROVALS:**

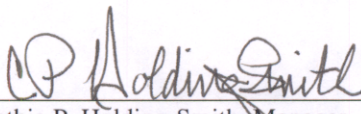
---

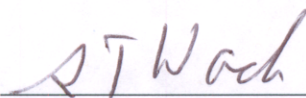
 DATE: 8-30-2001  
Chung Gong, Author  
Engineering Modeling & Simulation Group, Engineering Development Section

 DATE: 9/4/2001  
Mark A. Phifer, Technical Reviewer  
Environmental Restoration Technology Section, Environmental Science Technology Department

 DATE: 9/4/01  
William Eldon Jones, Customer  
Geo-Modeling Group, Environmental Restoration Technology Section

 DATE: 9/5/01  
Mary K. Harris, Manager  
Geo-Modeling Group, Environmental Restoration Technology Section

 DATE: 9/15/01  
Cynthia P. Holding-Smith, Manager  
Engineering Modeling & Simulation Group, Engineering Development Section

 DATE: 9/20/01  
Steven T. Wach, Manager  
Engineering Development Section, Engineered Equipment & System Department

# CONTENTS

<i>Executive Summary</i>	1
<i>Introduction</i>	2
<i>Background</i>	4
<i>Finite Element Analysis</i>	6
<i>Dynamic Compaction</i>	6
<i>Geometric Modeling</i>	6
<i>Material Modeling of the Impact Weight</i>	11
<i>The Material Model of Metals</i>	11
<i>Mathematical Modeling of Metals</i>	12
<i>The Mathematical Model of Soils</i>	14
<i>Strain Rate Decomposition</i>	15
<i>Elastic Behavior</i>	15
<i>Plastic Behavior</i>	15
<i>Material Modeling of Waste</i>	19
<i>Applied Load</i>	23
<i>Results</i>	23
<i>Determination of Time Increment in Explicit Integration</i>	24
<i>Deformation Characteristics of the B-25 Boxes</i>	25
<i>Time History of the Energies in the System</i>	36
<i>Pseudo-Engineering Stress Strain Curve in the Dynamic Compaction</i>	44
<i>Will Finer Finite Element Mesh Improve the Dynamic Compaction Results?</i>	48
<i>Conclusion</i>	65
<i>References</i>	69

## Nomenclature

<b>Symbol</b>	<b>Definition</b>	<b>Equation Number</b>
$E_{Impact-Weight}$	Modulus of elasticity of the Impact Weight	1
$E_{Steel}$	Modulus of elasticity of Steel	1
$MPa$	Mega Pascal	1
$\mathbf{F}$	Total deformation gradient	2
$\mathbf{F}^{el}$	Fully recoverable part of the deformation gradient	2
$\mathbf{F}^{pl}$	Plastic deformation gradient	2
$d\mathbf{e}$	Total strain rate tensor	3
$d\mathbf{e}^{el}$	Elastic strain rate tensor	3
$d\mathbf{e}^{pl}$	Plastic strain rate tensor (includes all inelastic strain rates)	3
$\mathbf{e}$	Total Strain tensor	4, 14
$\mathbf{e}^{el}$	Elastic strain tensor	4
$\mathbf{e}^{pl}$	Plastic strain (includes all inelastic strains) tensor	4
$K$	Bulk modulus	5, 7
$E$	Modulus of elasticity	5, 6
$\mathbf{n}$	Poisson's ratio	5, 6
$G$	Shear modulus	6, 9
$p$	Equivalent (hydrostatic) pressure stress	7, 8
$\mathbf{e}_{vol}$	Volumetric strain	7
$\mathbf{S}$	Cauchy stress tensor	8, 10
trace ( $\mathbf{S}$ )	Summation of the three principal components of the stress tensor $\mathbf{S}$ . In essence it can be expressed as: $trace(\mathbf{S}) = \mathbf{S}_{11} + \mathbf{S}_{22} + \mathbf{S}_{33}$	8
$\mathbf{S}$	Deviatoric stress tensor	9, 10, 11, 12
$\mathbf{e}^{el}$	Deviatoric elastic strain tensor	9
$\mathbf{I}$	Unit tensor or identity matrix, in the matrix notation: $\mathbf{I} = \begin{bmatrix} 1 & 0 & 0 \\ 0 & 1 & 0 \\ 0 & 0 & 1 \end{bmatrix}$	10, 14
$d\mathbf{e}^{pl}$	Deviatoric plastic strain rate	11
$d\bar{\mathbf{e}}^{pl}$	Equivalent plastic strain rate	11
$\dot{\mathbf{e}}^{pl}$	Deviatoric plastic strain rate tensor	13
$q$	von Mises Equivalent stress	12, 15
$dt$	Time increment	13
$\mathbf{e}$	Deviatoric strain tensor	14
$\mathbf{e}^{pl}$	Plastic strain tensor	14
trace( $\mathbf{e}^{pl}$ )	$trace(\mathbf{e}^{pl}) = \mathbf{I} : \mathbf{e}^{pl} = \mathbf{e}_{11}^{pl} + \mathbf{e}_{22}^{pl} + \mathbf{e}_{33}^{pl}$	14
$\mathbf{S}^0$	Yield stress that is a material parameter	15

$d\mathbf{e}$	Total strain rate tensor	16
$d\mathbf{e}^{el}$	Elastic strain rate tensor	16
$d\mathbf{e}^{pl}$	Inelastic (plastic) time-independent strain rate tensor	16
$d\mathbf{e}^{cr}$	Inelastic (creep) time-dependent strain rate tensor	16
$p$	Equivalent (hydrostatic) pressure stress	17, 20, 22, 23, 24
$trace(\mathbf{s})$	$trace(\mathbf{s}) = \mathbf{s} : \mathbf{I} = \mathbf{s}_{11} + \mathbf{s}_{22} + \mathbf{s}_{33}$	17
$q$	von Mises Equivalent stress	18
$\mathbf{S}$	Deviatoric stress tensor	18, 19, 20
$\mathbf{g}$	Third invariant of deviatoric stress tensor	19
$\mathbf{s}$	Cauchy stress tensor	17, 20
$\mathbf{I}$	Unit tensor or identity matrix, in the matrix notation: $\mathbf{I} = \begin{bmatrix} 1 & 0 & 0 \\ 0 & 1 & 0 \\ 0 & 0 & 1 \end{bmatrix}$	17, 20
$t$	A deviatoric stress measure that allows the matching of different stress values in tension and compression in the deviatoric plane (as sketched in Figure 8).	21, 22, 23, 25
$K$	A material parameter that varies between 0.778 and 1.0, the graphical effect of K is shown in Figure 8.	21
$F_s$	The Drucker-Prager failure surface (shear failure surface) (Figure 7)	22
$\mathbf{b}$	The material's angle of friction (Figure 7)	22, 23, 24, 25
$d$	The material's cohesion (Figure 7)	22, 23, 24, 25
$F_c$	The cap yield surface (Figure 7)	23
$p_a$	An evolution parameter that represents the volumetric plastic strain driven hardening/softening (Figure 7)	23, 24, 25
$R$	Material parameter that controls the shape of the cap (Figure 7)	23, 24
$\mathbf{a}$	A small number used to define a smooth transition surface between the shear failure surface and the cap (Figure 7)	23, 25
$p_b$	The hydrostatic compression yield stress (as shown in Figures 7, 9)	24,
$F_t$	The transition surface between the shear failure surface and the cap (Figure 7)	25
$\mathbf{e}_{vol}^{in}$	Inelastic volumetric strain	between 23, 24
$\mathbf{e}_{vol}^{in}  _0$	Initial value of inelastic volumetric strain (as shown in Figure 9)	between 23, 24

$\mathbf{e}_{vol}^{pl}$	Plastic volumetric strain	between 23, 24
$\mathbf{e}_{vol}^{cr}$	Creep volumetric strain	between 23, 24
$F$	Yield surface of crushable foams	26
$p$	Equivalent (hydrostatic) pressure stress (as shown in Figures 10, 11)	26
$p_t$	Strength of the material in hydrostatic tension (Figures 10, 11)	26, 27
$p_c$	Yield strength in hydrostatic compression (Figures 10, 11)	26
$t$	A deviatoric stress measure that allows the matching of different stress values in tension and compression in the deviatoric plane as sketched in Figures 10 and 11.	26
$M$	The slope of the critical state line in the $p$ - $t$ plane (Figure 10)	26, 27
$p_{c/0}$	Initial value of the yield strength in hydrostatic compression (Figures 10, 11)	27
$\mathbf{s}_0$	Initial yield strength in uniaxial compression (Figure 10)	27
$\mathbf{e}_{vol}^{pl}$	Plastic volumetric strain (Figure 11)	
$\mathbf{e}_{vol}^{pl}  _0$	Initial value of the plastic volumetric strain (Figure 11)	
$V_{Impact\_weight}$	The initial velocity of the Impact Weight	28
$g$	The gravitational acceleration	28, 29
$h$	The height from which the impact weight dropped	28, 29
$M$	Mass of the impact weight	29
$N\ m$	Newton-meter, the energy unit	29
$ v $	Absolute value of the wave speed in a medium	30
$\mathbf{D}$	Time increment	30
$\mathbf{D}\kappa$	Nominal linear size of a finite element	30
$S$	Pseudo-engineering stress	31
$a_3$	Vertical component of deceleration at the bottom of the impact weight	31
$A$	Area of the contact surface between the bottom of the impact weight and the top lid surface of the top B-25 box in the stack	31
$M$	Mass of the impact weight	31
$\mathbf{e}$	Pseudo-engineering strain	32
$u$	Vertical component of displacement at the bottom of the impact weight	32
$H$	The undeformed height of the stack of four B-25 boxes	32



## ***List of Figures***

<b><i>Figure</i></b>	<b><i>Caption</i></b>	<b><i>Page</i></b>
Figure 1.	The Finite Element Mesh of the Impact Weight	7
Figure 2.	Isometric Top View of a Finite Element Analysis Model of a B-25 Box	8
Figure 3.	Isometric Bottom View of a Finite Element Analysis Model of a B-25 Box	8
Figure 4.	The Soil Foundation Modeled with Solid Continuum Elements	9
Figure 5.	Four B-25 Boxes Standing on Top of the Soil Foundation	10
Figure 6.	Two B-25 Boxes with Side Panels Removed to Show the Waste Inside	11
Figure 7.	Modified Drucker-Prager / Cap model: Yield Surfaces in the $p-t$ Plane	14
Figure 8.	Typical yield / Flow Surfaces in the Deviatoric Plane	16
Figure 9.	Typical Cap Hardening	18
Figure 10.	Yield Surfaces in the $p-t$ Plane for the Foam Model	20
Figure 11.	Typical Hardening / Softening Rule for the Foam Model	21
Figure 12.	Volumetric Strain Hardening Curves for the Two Waste Models	22
Figure 13.	Deformation Configuration of a Stack of B-25 Boxes	26
Figure 14.	Top View of the Deformed B-25 Box (Box 4) at the Top of the Stack	27
Figure 15.	Bottom View of the Deformed B-25 (Box 4) Box at the Top of the Stack	28
Figure 16.	Top View of the Deformed B-25 (Box 3) Box Positioned Next from the Top of the Stack	30
Figure 17.	Bottom View of the Deformed B-25 (Box 3) Box Positioned Next from the Top of the Stack	30
Figure 18.	Top View of the Deformed B-25 (Box 2) Box Positioned Next from the Bottom of the Stack	31
Figure 19.	Bottom View of the Deformed B-25 (Box 2) Box Positioned Next from the Bottom of the Stack	31
Figure 20.	Top View of the Deformed Bottom B-25 (Box 1) Box in the Stack	33
Figure 21.	Bottom View of the Deformed Bottom B-25 (Box 1) Box in the Stack	33
Figure 22.	Deformed Soil Foundation	34
Figure 23.	Top View of Two Deformed Top B-25 Boxes (Boxes 3 and 4) in the Stack with Waste Inside	35
Figure 24.	Top View of Two Deformed Bottom B-25 Boxes (Boxes 1 and 2) in the Stack with Waste Inside	35
Figure 25.	The Interior of the Stack of Deformed B-25 Boxes	36
Figure 26.	Time History of Kinetic Energy, Dissipated Plastic Energy and Elastic Strain Energy in the Whole Mechanical System	37

Figure 27.	Time History of Kinetic Energy, Dissipated Plastic Energy and Elastic Strain Energy in the Stack of Four B-25 Boxes and Waste inside the Boxes	38
Figure 28.	Top View of the Deformed B-25 Box (Box 3, second from the top of the stack) in the First 0.04 Seconds during the Dynamic Compaction	39
Figure 29.	Top View of the Deformed B-25 Box (Box 3, second from the top of the stack) in the Last 0.09 Seconds during the Dynamic Compaction	40
Figure 30.	Bottom View of the Deformed B-25 Box (Box 3, second from the top of the stack) in the First 0.04 Seconds during the Dynamic Compaction	41
Figure 31.	Bottom View of the Deformed B-25 Box (Box 3, second from the top of the stack) in the Last 0.09 Seconds during the Dynamic Compaction	42
Figure 32.	The Complete Pseudo-Engineering Stress Strain Curve for the Dynamic Compaction of a Stack of Four B-25 Boxes with Waste Inside the Boxes	45
Figure 33.	The Truncated Pseudo-Engineering Stress Strain Curve for the Dynamic Compaction of a Stack of Four B-25 Boxes with Waste Inside the Boxes	47
Figure 34.	Isometric Top View of a Finite Element Analysis Model with Refined Mesh of a Stack of Four B-25 Boxes	49
Figure 35.	Isometric Top View of a Finite Element Analysis Model with Refined Mesh of one B-25 Box	50
Figure 36.	Isometric Top View of the Deformed Stack of Four B-25 Boxes that modeled with Refined Finite Element Mesh and Calculated with Code-determined Time Increment	51
Figure 37.	Isometric Top View of the Deformed B-25 Box (Box 4) on the Top of the Stack modeled with Refined Finite Element Mesh and Calculated with Code-determined Time Increment	52
Figure 38.	Isometric Bottom View of the Deformed B-25 Box (Box 4) on the Top of the Stack modeled with Refined Finite Element Mesh and Calculated with Code-determined Time Increment	52
Figure 39.	Isometric Top View of the Deformed B-25 Box (Box 3) Second from the Top of the Stack modeled with Refined Finite Element Mesh and Calculated with Code-determined Time Increment	53
Figure 40.	Isometric Bottom View of the Deformed B-25 Box (Box 3) Second from the Top of the Stack modeled with Refined Finite Element Mesh and Calculated with Code-determined Time Increment	53
Figure 41.	Isometric Top View of the Deformed B-25 Box (Box 2) Second from the Bottom of the Stack modeled with Refined Finite Element Mesh and Calculated with Code-determined Time Increment	54
Figure 42.	Isometric Bottom View of the Deformed B-25 Box (Box 2) Second from the Bottom of the Stack modeled with Refined Finite Element Mesh and Calculated with Code-determined Time Increment	54
Figure 43.	Isometric Top View of the Deformed B-25 Box (Box 1) at the Bottom of the Stack modeled with Refined Finite Element Mesh and Calculated with Code-determined Time Increment	55

Figure 44.	Isometric Bottom View of the Deformed B-25 Box (Box 1) at the Bottom of the Stack modeled with Refined Finite Element Mesh and Calculated with Code-determined Time Increment	55
Figure 45.	Isometric Top View of the Deformed Stack of Four B-25 Boxes modeled with Refined Finite Element Mesh and Calculated with Fixed Time Increment	56
Figure 46.	Isometric Top View of the Deformed B-25 Box (Box 4) on the Top of the Stack modeled with Refined Finite Element Mesh and Calculated with Fixed Time Increment	57
Figure 47.	Isometric Bottom View of the Deformed B-25 Box (Box 4) on the Top of the Stack modeled with Refined Finite Element Mesh and Calculated with Fixed Time Increment	57
Figure 48.	Isometric Top View of the Deformed B-25 Box (Box 3) Second from the Top of the Stack modeled with Refined Finite Element Mesh and Calculated with Fixed Time Increment	58
Figure 49.	Isometric Bottom View of the Deformed B-25 Box (Box 3) Second from the Top of the Stack modeled with Refined Finite Element Mesh and Calculated with Fixed Time Increment	58
Figure 50.	Isometric Top View of the Deformed B-25 Box (Box 2) Second from the Bottom of the Stack modeled with Refined Finite Element Mesh and Calculated with Fixed Time Increment	59
Figure 51.	Isometric Bottom View of the Deformed B-25 Box (Box 2) Second from the Bottom of the Stack modeled with Refined Finite Element Mesh and Calculated with Fixed Time Increment	59
Figure 52.	Isometric Top View of the Deformed B-25 Box (Box 1) at the Bottom of the Stack modeled with Refined Finite Element Mesh and Calculated with Fixed Time Increment	60
Figure 53.	Isometric Bottom View of the Deformed B-25 Box (Box 1) at the Bottom of the Stack modeled with Refined Finite Element Mesh and Calculated with Fixed Time Increment	60
Figure 54.	Time History of Kinetic Energy, Dissipated Plastic Energy and Elastic Strain Energy in the Whole Mechanical System Modeled with refined Mesh	61
Figure 55.	Time History of Kinetic Energy, Dissipated Plastic Energy and Elastic Strain Energy in the Stack of Four B-25 Boxes and Waste inside the Boxes Modeled with Refined Mesh	62
Figure 56.	Time History of Kinetic Energy in the Stack of Four B-25 Boxes and Waste inside the Boxes Modeled with Both Fine and Refined Meshes	63
Figure 57.	Time History of Dissipated Plastic Energy, in the Stack of Four B-25 Boxes and Waste inside the Boxes Modeled with Both Fine and Refined Meshes	64
Figure 58.	Time History of Elastic Strain Energy, in the Stack of Four B-25 Boxes and Waste inside the Boxes Modeled with Both Fine and Refined Meshes	65

## *List of Tables*

Table 1.	The Dimensions of the B-25 Box	7
Table 2.	Parameters for the Drucker-Prager/Cap Plasticity Model	19
Table 3.	Parameters for the Crushable Foam Plasticity Models of the Waste	22
Table 4.	Distribution of Waste in the B-25 Boxes in the Stack	23
Table 5.	Number of Elements and Nodal Points in the Model	24
Table 6.	Number of Elements and Nodal Points in the Refined Model	48
Table 7.	Time Increments and CPU Times for Three Computational Models	49

## **FINITE ELEMENT ANALYSIS OF DYNAMIC COMPACTION OF A STACK OF FOUR B-25 BOXES (U)**

### ***Executive Summary***

The Engineered Trench is one of the facilities at SRS that provide containment to reduce radionuclide migration from disposed Low-Level Waste (LLW) forms. The LLW will be containerized in B-25 boxes. The B-25 boxes are placed into the excavated-engineered trench in stacks. There are four B-25 boxes in each stack. After the trench is filled with stacks of B-25 boxes, a 1.2-meter interim soil cover will be placed on top of the B-25 boxes. On top of the interim soil cover a closure cap will be installed to minimize moisture contact with the waste.

The void space of the waste in the B-25 boxes varies greatly from 10% to 90%. The mass density of the waste in the B-25 boxes also has a wide range of variation. The mechanical strength of the waste in each of the boxes cannot be determined.

Dynamic compaction is one of the mechanical methods to reduce the void spaces in the B-25 boxes. The effectiveness of dynamic compaction varies with many factors. The strength of the boxes, the relative hardness of the waste inside boxes, the soil foundation as well as the soil cover over the stack of boxes are the direct influential factors that control the deformation configuration of the boxes. The tidiness in stacking the boxes and corrosion in the boxes will also alter the results of dynamic compaction.

This analysis intends to establish a framework for the comprehensive parametric study of the mechanical behaviors of the stack of B-25 boxes and consequently the whole engineered trench with closure cap.

The stack of four B-25 boxes with waste inside are modeled with finite elements. The stack of boxes is sitting on the top of a soil foundation. Three different material models are developed in this analysis. The elasto-plastic model with strain hardening is for carbon steel that is the material for the B-25 boxes. The waste is modeled with crushable foam that is similar to the cellular solids. The Drucker-Prager model with cap is the most proper constitutional function for soils.

With testing data for the materials available, the finite element analysis will provide reasonably reliable solution to the problems. For the purpose of parametric studies, the mathematical models established in this report would offer sufficient flexibility in varying all the possible parameters.

Two grades of finite element mesh sizes were developed in this analysis for comparison. Also two time increment scales were used in the explicit time integration. The finite element code, based upon the mesh size and material properties would compute the



maximum time increment for numerical stability. Through experience and understanding of the propagation of mechanical waves, a fixed time increment can be determined for more accurate calculation.

The deformation configurations of the B-25 boxes from the three computations provide realistic pictures for the mechanical behaviors of the system. However, the calculation for the model with refined mesh and fixed time increment consumes excessive CPU time (339,611 seconds). While with the fine mesh model and fixed time, the CPU time for the calculation takes only 75,539 seconds (about 4.5 times less). The later model will be used for further parametric studies.

In addition to the realistic deformation configurations, the time history of energies and the pseudo-engineering stress-strain curves also provide important information for the understanding of the mechanical behaviors of the box system.

The deformation configuration is different for B-25 boxes at different locations in the stack and it is also different for different relative stiffness of the soil foundation. For a foundation with absorbing materials, the dynamic impact transmitted into the foundation may have much less energy being reflected back to the boxes. Then the top B-25 boxes would show more damage. In this analysis, the foundation material is relatively stiff when it is confined at the bottom of the box. Consequently, the bottom of the B-25 in contact with the foundation is crushed inward.

This analysis indicates that a numerical parametric study is a reliable and feasible tool in determining the best choice for waste disposition methods.

## ***Introduction***

The Engineered Trench is one of the facilities at SRS that provides containment to reduce radionuclide migration from disposed Low-Level Waste (LLW) forms. The LLW will be containerized in B-25 boxes. The B-25 boxes are placed into the excavated-engineered trench in stacks. There are four B-25 boxes in each stack. After the trench is filled with stacks of B-25 boxes, a 1.2-meter interim soil cover will be placed on top of the B-25 boxes. On top of the interim soil cover a closure cap will be installed to minimize moisture contact with the waste.

The void space of the waste in the B-25 boxes varies greatly from 10% to 90%. The mass density of the waste in the B-25 boxes also has a wide range of variation. The mechanical strength of the waste in each of the boxes cannot be determined.

During a long-term (from 100-year to 1,000-year) disposal of the waste inside the engineered trench, the void spaces in the containerized waste will be gradually reduced due to the following factors:

1. Corrosion of the B-25 boxes that induces collapse of the stack of boxes;
2. Degradation of the waste that reduces the volume of the waste;
3. Overburden loads that compress the stack of boxes.

In order to accelerate the void-space reduction of the stack of B-25 boxes, static and/or dynamic pre-compaction of the box stacks may be applied. For more efficient void-space reduction, the dynamic compaction and/or static surcharge may be postponed until the B-25 boxes have corroded significantly

This analysis intends to evaluate the feasibility of developing a numerical model for the dynamic compaction process. A realistic mathematical model of the stack of four B-25 boxes will be constructed. In the system, besides the carbon steel for the boxes, the material models for the waste and the foundation soil are also developed. In addition to providing a detailed explanation of the mechanical behaviors of the B-25 boxes during dynamic impact, this analysis also institutes a list of material parameters required for this type of calculations.

The mechanical properties of the major materials (viz., steel, soil and waste) in this analysis vary with space and time. Massive parametric analyses are needed for the understanding of the effects of various compaction methods on the subsidence of the trench cover. The methodology developed in this analysis will be applied to the parameter studies in other cases. Numerical computation with finite element analysis technique is a feasible tool to deal with this type of problem.

In a dynamic impact process, the structural system experiences highly nonlinear deformation. Mechanical (elastic and plastic) waves propagate in the whole structural system. The details of the geometric configuration and material properties of the system will influence the final results of the calculation. The important factors are:

1. Geometric configuration;
2. Kinematic boundary conditions;
3. Kinematic initial conditions;
4. Mechanical properties of materials;
5. Modeling and computational techniques.

In the engineered trench hundreds of stacks of B-25 boxes are closely packed side to side. The distribution of waste inside the boxes is completely random. On the top of the box stacks a layer of soil is loosely deposited. During the dynamic compaction, the relative location of the impact weight to each stack is not measured. In the real dynamic compaction process, the material properties as well as all the kinematic conditions are not completely determined

Practically it is impossible to control and optimize the waste-distribution and box stacking in the trench. Theoretically, in order to have a comprehensive understanding of the mechanical influence from the randomness of all these physical parameters, a

thorough stochastic analysis should be performed. Unfortunately the present computational facility will not allow a sufficiently stochastic dynamic analysis.

From the finite element analysis results (Static or Dynamic Compaction Calculations), the pseudo stress-strain relations in a stack of four B-25 boxes can be derived [Gong, 2000]. These pseudo stress-strain curves will serve as useful information for the analysis of the engineering trenches.

After reviewing the background of this project, the numerical modeling technique will be expounded in detail. The results obtained from this analysis of dynamic compaction are illustrated with deformation configurations and time history curves. The geometric and material models are sufficiently flexible and versatile such that the same modeling technique can be applied to problems with different degrees of corrosion, geometry and material properties. The deformation configuration of the stack of four B-25 boxes shows the mechanical effects of the impact weight and the response from the soil foundation.

## ***Background***

The overall objective of the Department of Energy (DOE) order DOE O 435.1 Radioactive Waste Management and its companion manual (DOE M 435.1-1) and implementation guide (DOE G 435.1-1) in relation to disposal facilities is to protect the public, environment, and workers and to comply with the stated performance objectives. This objective is realized by specific requirements designed to minimize the transport of radionuclides from the disposal facilities. Minimization of the subsidence of the engineered trench cap is one such requirement. Subsidence should be minimized, since it may lead to increase water infiltration into the waste, which in turn may lead to an increased release of radionuclides to the environment.

DOE M 435.1-1, Radioactive Waste Management Manual, Chapter IV, Low-Level Waste Requirement, Section P, Disposal, Item (6), Disposal Facility Operation states the following regarding operations of low-level radioactive waste disposal facilities in relation to the minimization of subsidence:

- (a) Operating procedures shall be developed and implemented for low-level waste disposal facilities that ... minimize subsidence during and after waste emplacement; achieve long-term stability and minimize the need for long-term active maintenance...
- (b) Low-level waste placement into disposal units shall minimize voids between waste containers. Voids within disposal units shall be filled to the extent practical. Un-containerized bulk waste shall also be placed in a manner that minimizes voids and subsidence.

At SRS and other DOE sites, wastes in containers that have from 10% to 90% void space are disposed in shallow land burial facilities. Corrosion and degradation of these

containers combined with the void space between containers can result in significant subsidence in time. Subsidence, in turn, can lead to increased water infiltration through the long-term cover into the waste and subsequently increase radionuclide transport into the environment.

A three-year study is being implemented to improve our understanding of the impacts of waste and container degradation on trench and closure cover subsidence and subsequent system performance. The Subsurface Contaminants Focus Area (SCFA) is funding this study. The overall objective is to develop a design methodology to evaluate waste stabilization options and to select the most appropriate option for implementation. This design methodology will be integrated into the SCFA Long Term Capping Technical Program Strategy, whose output will be the production of a DOE Long Term Capping Design Guideline, which will provide complex-wide guidance for long-term capping.

The evaluation and selection process will be based upon the impact of the waste physical stabilization options on long-term structural stability, subsidence, long-term active maintenance, cost effectiveness, and the associated risk as evaluated against DOE Order O 435.1 Performance Objectives through integration with the Performance Assessment Process.

This design methodology will be developed through a case study of the SRS Engineered Trench Low-level Radioactive Waste Disposal Facility. The Engineered Trench uses B-25 boxes for waste disposal and assumes use of dynamic compaction and a kaolin cap for closure as the baseline.

Detailed expositions about the Low-Level Waste Disposal and Trench Subsidence Evaluation can be found in the following documents:

1. Phifer, M. A., Serrato, M. G., 2000, "Preliminary E-area Trench Subsidence Evaluation", Inter-Office Memorandum to L. C. Thomas, SRT-EST-2000-00105, January 18, 2000.
2. Phifer, M. A., 2000, "Technical Task Plan (TTP): Long-term Waste Stabilization Design for Long-term Cover Systems", SR1-1-SS-99, March 28, 2000.
3. Butcher, B. T., Wilhite, E. L., and Phifer, M. A., (SRTC), and Thomas, L. C., and Goldston, W. T. (SWD), 2000, "Program Plan for Evaluating Trench Disposal of Uncompacted Job Control Waste", SRT-WED-2000-00044, Rev. 0, December 4, 2000.
4. Wilhite, E. L., 2000, "Evaluation of Proposed New LLW Disposal Activity Disposal of LLW in a Mega Trench rather than in Slit Trenches", WSRC-RP-2000-00217, May 4, 2000.
5. Phifer, M. A., 2000, "Technical Task Plan (TTP): Long-term Waste Stabilization Design for Long-term Cover Systems", SR1-1-SS-29, July 24, 2000.

6. Jones, W. E., Gong, C., Dunn, K. A., 2001, "Scoping Study Plan: Long-term Waste Stabilization Design for Long-term Cover Systems", TTP SR11SS29, SRT-EST-2001-0000105, January 2001.

## ***Finite Element Analysis***

The commercially available finite element analysis code, ABAQUS<sup>®</sup> [HKS, 1998] has been selected for use based upon the present budget and the adequacy of the code for this purpose. ABAQUS<sup>®</sup> is a general-purpose nonlinear finite element program, which is developed and maintained by Hibbitt, Karlsson and Sorensen, Inc. This program is continuously in the process of modification and improvement as well as bug-removal. The version we used for this calculation is version 5.8-1N. This is a nuclear quality assurance (QA) version [Gong, 1999a]. In the middle of this year, 2001, a new version (version 6.2) of ABAQUS<sup>®</sup> will be available at SRS. The new version of ABAQUS<sup>®</sup> will be used for later calculations.

In finite element analysis, there are two major numerical integration methods in practice [Hughes, 1987]. Depending on the amount of calculations and the computer size, we can choose either implicit integration or explicit integration technique. For this dynamic compaction analysis of B-25 boxes, the explicit integration method is adopted. The finite element mesh of the model is generated by using the graphic software, MSC/PATRAN<sup>®</sup>, version 8.5 [MSC, 1999].

## ***Dynamic Compaction***

### ***Geometric Modeling***

In this analysis three structural components are modeled, namely,

1. Impact weight;
2. Four B-25 boxes;
3. Trench foundation.

The impact weight is in the shape of a circular cylinder with 8-foot (2.4384-meter) in diameter [McMullin, 1994]. In this calculation, the height of the impact weight is not important, rather the entire mass and the diameter of the contact surface are essential in the dynamic compaction process. The impact weight is modeled with a 0.2 meter thick (0.66 feet) 2.4384 (8-foot) diameter circular disk, which has a volume of 0.93396 cubic meter. The finite element mesh of the impact weight is depicted in Figure 1.



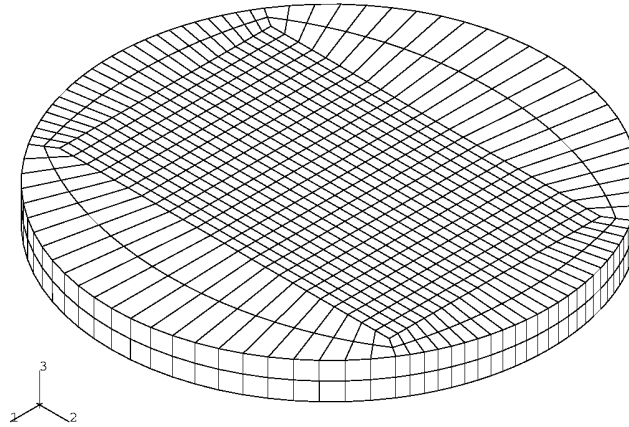


Figure 1. The Finite Element Mesh of the Impact Weight.

The mass of the impact weight is 20 tons (18,100 kilograms) [McMullin, 1994] that gives equivalent mass density of 19,379.778 kg per cubic meter. Since the stress distribution in the impact weight is not of concern in this analysis, the modulus of elasticity of the impact weight can be modified such that the mechanical wave speed in the circular disk remains the same as the impact weight would maintain its original dimensions. The impact weight is modeled with 3-D solid continuum elements.

The B-25 box has the exterior dimensions as shown in Table 1 [1987, Procurement Specification, 2000]:

Table 1. The Dimensions of the B-25 Box

<b><i>Exterior Dimensions</i></b>	<b><i>Meter</i></b>
<i>Length</i>	<i>1.84</i>
<i>Width</i>	<i>1.18</i>
<i>Height (Not including riser)</i>	<i>1.20</i>
<i>Riser Height</i>	<i>0.10</i>
<i>Thickness (12 gauge)</i>	<i>0.00265684</i>

Each of the B-25 boxes is modeled with 5040 3-D shell elements that are connected with 4985 nodes. A B-25 box is depicted in Figures 2 and 3.

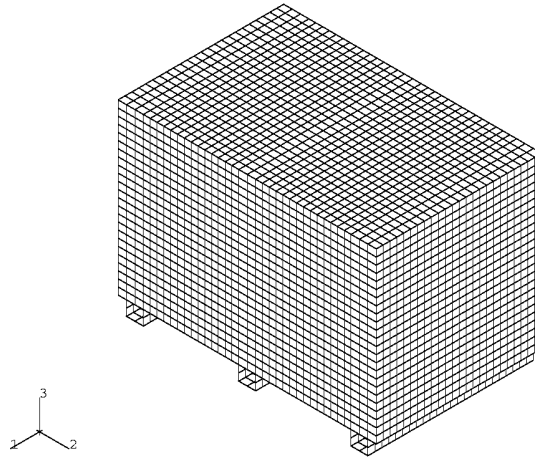


Figure 2. Isometric Top View of a Finite Element Analysis Model of a B-25 Box

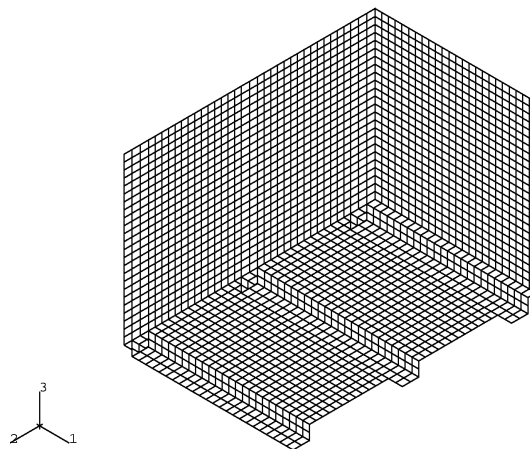


Figure 3. Isometric Bottom View of a Finite Element Analysis Model of a B-25 Box

The soil foundation is meshed with 3-D solid continuum elements as a truncated pyramid that is shown in Figure 4.

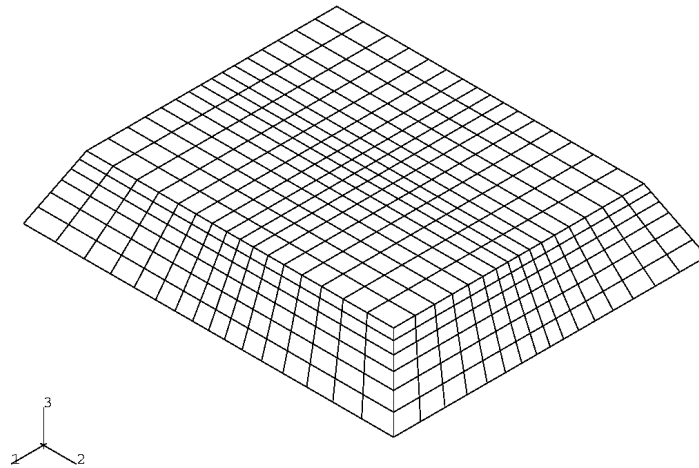


Figure 4. The Soil Foundation Modeled with Solid Continuum Elements.

Four B-25 boxes are modeled in a vertical stack. The stack of B-25 boxes on top of the foundation is shown in Figure 5.

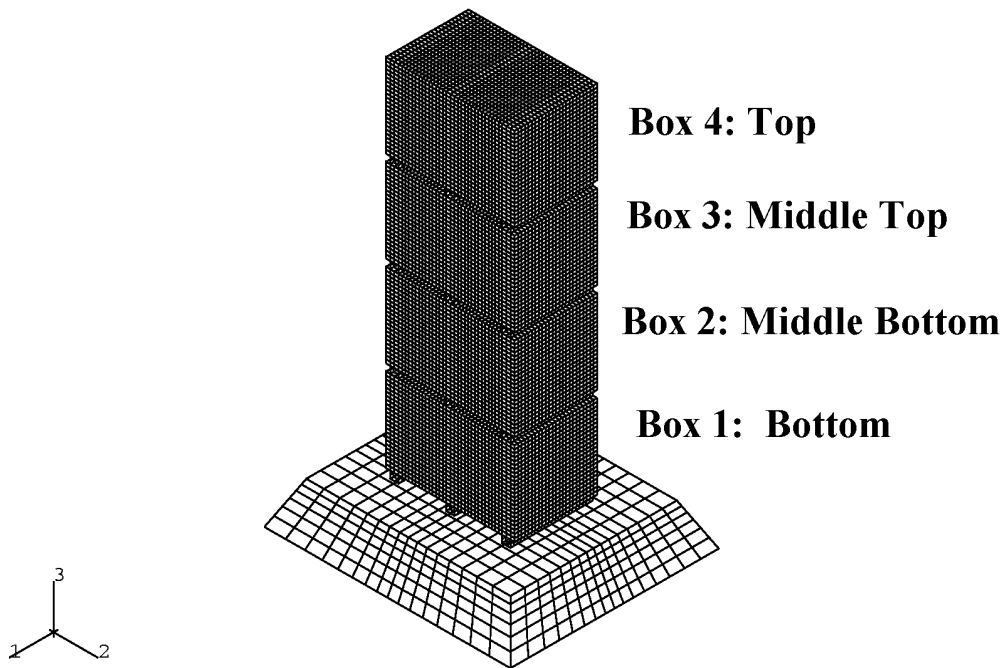


Figure 5. Four B-25 Boxes Standing on Top of the Soil Foundation

Inside each of the B-25 boxes, the waste is modeled with 3-D solid continuum elements. Each of the B-25 boxes is half filled with waste. Two boxes with side panels removed such that the waste inside the boxes can be displayed are shown in Figure 6.

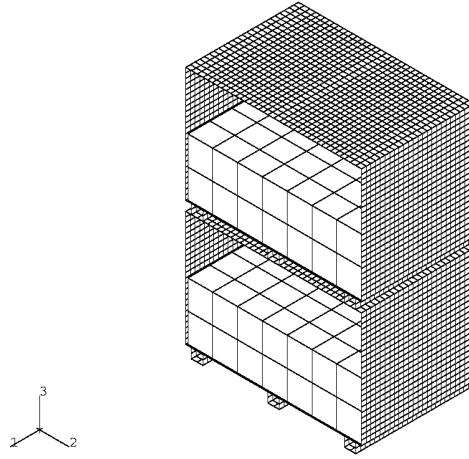


Figure 6. Two B-25 Boxes with Side Panels Removed to Show the Waste Inside.

### ***Material Modeling of the Impact Weight***

By matching the original mechanical wave velocity in the reduced impact weight, the modulus of elasticity of the impact weight is increased more than 2.5 times as that of steel. The density of steel is 7,500 kg per cubic meter.

$$E_{Impact-Weight} = MassDensityRatio \times E_{Steel} = \frac{19,379.778}{7,500} \times 206,842.8 MPa = 534,475.7 MPa \quad (1)$$

With this high modulus of elasticity as compared with that of the B-25 boxes, the impact weight behaves literally as a rigid body during the dynamic compaction process.

### ***The Material Model of Metals***

The isotropic rate-independent elastic-plastic mechanical properties for metals will be used in this analysis.

The B-25 boxes are made of hot rolled low-carbon steel sheets. The density of steel is 7,500 kg/meter<sup>3</sup>. The modulus of elasticity is approximately 200,000 MPa, with a Poisson's ratio of 0.28. The yield strength is 220.63232 MPa. The true ultimate tensile strength is 385.623927 MPa at the ultimate true strain of 17.4% [ASM, 1961, 1990]. The



plasticity of the steel is monitored by the von Mises yield criterion for metals with isotropic hardening and associated flow rule [Hill, 1950, Malvern, 1969].

### ***Mathematical Modeling of Metals***

To reduce the void spaces in the B-25 boxes through dynamic compaction depends on the induction of permanent mechanical deformation in the boxes. Permanent deformation of a mechanical system is mathematically modeled with the theory of plasticity [Hill, 1950]. The mathematical modeling of the inelastic behaviors of the soil and waste will be discussed in sequel. Comparatively the metal plasticity is much simpler.

A basic assumption of elastic-plastic model is that the deformation can be divided into an elastic part and an inelastic (plastic) part. In its most general form this statement is written as

$$\mathbf{F} = \mathbf{F}^{el} \cdot \mathbf{F}^{pl} \quad (2)$$

Where  $\mathbf{F}$  is the total deformation gradient,  $\mathbf{F}^{el}$  is the fully recoverable part of the deformation at the point under consideration, and  $\mathbf{F}^{pl}$  is the plastic deformation gradient.

This decomposition can be used directly to formulate the plasticity model. The corresponding strain rate,  $d\mathbf{e}$ , decomposition is

$$d\mathbf{e} = d\mathbf{e}^{el} + d\mathbf{e}^{pl}. \quad (3)$$

Using the standard definition of corotational measures, this can be written in the integrated form as

$$\mathbf{e} = \mathbf{e}^{el} + \mathbf{e}^{pl} \quad (4)$$

The elasticity is linear and isotropic and therefore, can be written in terms of two temperature-dependent material parameters. The two material parameters are the bulk modulus,  $K$ , and the shear modulus  $G$ . These can be computed from the modulus of elasticity,  $E$ , and Poisson's ratio,  $\nu$ , as

$$K = \frac{E}{3(1 - 2\nu)}, \quad (5)$$

and

$$G = \frac{E}{2(1 + \nu)}. \quad (6)$$

Then the elasticity can be written in volumetric and deviatoric components as follows.

Volumetric: 
$$p = -K \mathbf{e}_{vol}, \quad (7)$$

where 
$$p = -\frac{1}{3} \text{trace}(\mathbf{S}) = -\frac{1}{3} \mathbf{S} : \mathbf{I} \quad (8)$$

is the equivalent (hydrostatic) pressure stress and  $\mathbf{S}$  is the Cauchy stress tensor.  $\mathbf{I}$  is the unit tensor (or the identity matrix).

Deviatoric: 
$$\mathbf{S} = 2G \mathbf{e}^{el} \quad (9)$$

where  $\mathbf{S}$  is the deviatoric stress,

$$\mathbf{S} = \mathbf{s} + p \mathbf{I} \quad (10)$$

The flow rule is

$$d\mathbf{e}^{pl} = d\bar{\epsilon}^{pl} \left( \frac{3}{2} \frac{\mathbf{S}}{q} \right) \quad (11)$$

where

$q$  is the von Mises equivalent stress

$$q = \sqrt{\frac{3}{2} \mathbf{S} : \mathbf{S}}, \quad (12)$$

$d\bar{\epsilon}^{pl}$  is the (scalar) equivalent strain rate

$$d\bar{\epsilon}^{pl} = \sqrt{\frac{2}{3} \dot{\mathbf{e}}^{pl} : \dot{\mathbf{e}}^{pl}} dt, \quad (13)$$

and  $\mathbf{e}$  is the deviatoric strain

$$\mathbf{e} = \mathbf{e} - \frac{1}{3} \mathbf{I} : \mathbf{e} \mathbf{I}. \quad (14)$$

In the plastic state the trace ( $\mathbf{e}^{pl}$ ) =  $\mathbf{I} : \mathbf{e}^{pl}$  is zero, i.e., the material is incompressible in the plastic state.

The plasticity requires that the material satisfy a uniaxial-stress , plastic-strain and strain-rate relationship. If the material is rate independent, this is the yield condition:

$$q = \mathbf{s}^0 \quad (15)$$

Where  $\mathbf{s}^0(\bar{\epsilon}^{pl}, \mathbf{q})$  is the yield stress that is a material parameter and is a function of equivalent plastic strain ( $\bar{\epsilon}^{pl}$ ) and temperature ( $\mathbf{q}$ ).

Numerical modeling of the elasto-plastic material can be found in the theory manual of ABAQUS<sup>®</sup> [HKS, 1998].

For certain crushable materials stored inside the containers, special mathematical models will be developed when the mechanical properties of those materials are available.

The waste blocks inside B-25 boxes are modeled with crushable foams. The real material properties of the waste are unknown.

The soil foundation is modeled with Drucker-Prager with Cap model for geological materials. Since, for the time being, the true testing data are not available; the parameters for this soil model are chosen based upon previous experience [Gong, 1993].

### *The mathematical model of soils*

The modified Drucker-Prager/Cap plasticity model in ABAQUS is intend for geological materials that exhibit pressure-dependent yield. The yield surface includes two main segments: a shear failure surface, providing dominantly shearing flow, and a “cap,” which intersects the equivalent pressure stress axis (Figure 7)

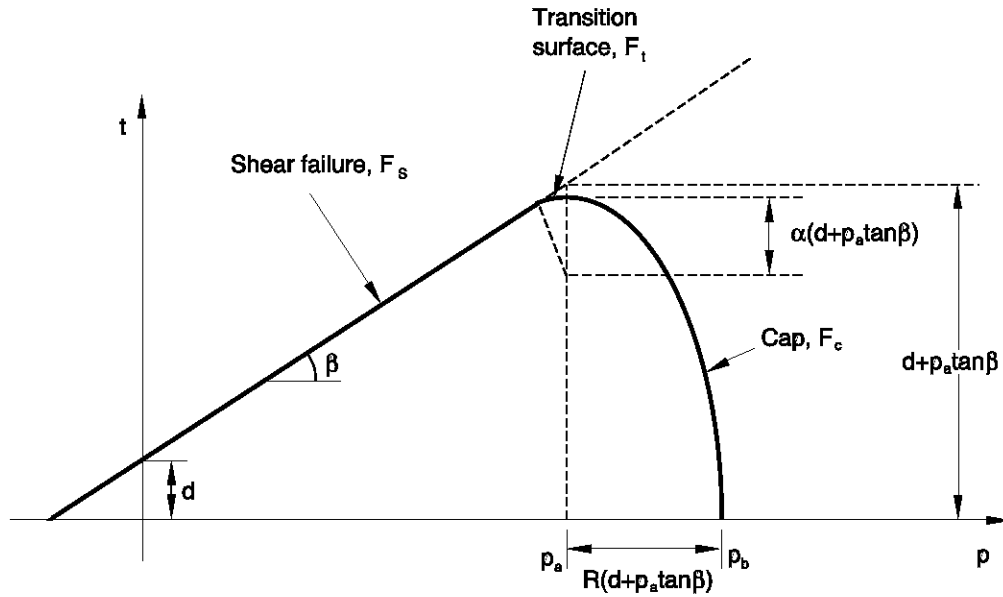


Figure 7. Modified Drucker-Prager / Cap Model: Yield Surfaces in the  $p$ - $t$  Plane.

There is a transition region between these segments, introduced to provide a smooth surface. The cap serves two main purposes: it bounds the yield surface in hydrostatic compression, thus providing an inelastic hardening mechanism to represent plastic

compaction, and it helps to control volume dilatancy when the material yields in shear by providing softening as a function of the inelastic volume increase created as the material yields on the Drucker-Prager shear failure and transition yield surfaces.

The model uses associated flow rule in the cap region and non-associated flow rule in the shear failure and transition regions. The model has been extended to include creep, with certain limitations. The creep behavior is envisaged as arising out of two possible mechanisms: one dominated by shear behavior and the other dominated by hydrostatic compression.

### ***Strain Rate Decomposition.***

A linear strain rate decomposition is assumed, so

$$d\mathbf{e} = d\mathbf{e}^{el} + d\mathbf{e}^{pl} + d\mathbf{e}^{cr} \quad (16)$$

where  $d\mathbf{e}$  is the total strain rate,  $d\mathbf{e}^{el}$  is the elastic strain rate,  $d\mathbf{e}^{pl}$  is the inelastic (plastic) time-independent strain rate, and  $d\mathbf{e}^{cr}$  is the inelastic (creep) time-dependent strain rate.

### ***Elastic Behavior.***

The elastic behavior can be modeled as linear elastic.

### ***Plastic Behavior.***

The yield/failure surfaces used with this model are written in terms of the three stress invariants: the equivalent pressure stress,

$$p = -\frac{1}{3}\text{trace}(\mathbf{S}) = -\frac{1}{3}\mathbf{S} : \mathbf{I}; \quad (17)$$

the von Mises equivalent stress,

$$q = \sqrt{\frac{3}{2}(\mathbf{S} : \mathbf{S})}; \quad (18)$$

and the third invariant of deviatoric stress

$$\mathbf{g} = \left( \frac{9}{2} \mathbf{S} \cdot \mathbf{S} : \mathbf{S} \right)^{\frac{1}{3}} \quad (19)$$

where  $\mathbf{S}$  is the stress deviator, defined as

$$\mathbf{S} = \mathbf{s} + p\mathbf{I} \quad (20)$$

We also define the deviatoric stress measure

$$t = \frac{q}{2} \left[ 1 + \frac{1}{K} - \left( 1 - \frac{1}{K} \right) \left( \frac{g}{q} \right)^3 \right] \quad (21)$$

where  $K(q, f^a)$  is a material parameter that may depend on temperature,  $q$  and other predefined field parameters. This measure of deviatoric stress is used because it allows matching of different stress values in tension and compression in the deviatoric plane, thereby providing flexibility in fitting experimental results and a smooth approximation to the Mohr-Coulomb surface. When  $K = 1$ , the dependence on the third deviatoric stress invariant is removed; and the von Mises circle is recovered in the deviatoric plane:  $t = q$ . Figure 8. Shows the dependence of  $t$  on  $K$ . To ensure convexity of the yield surface,  $0.778 \leq K \leq 1.0$ .

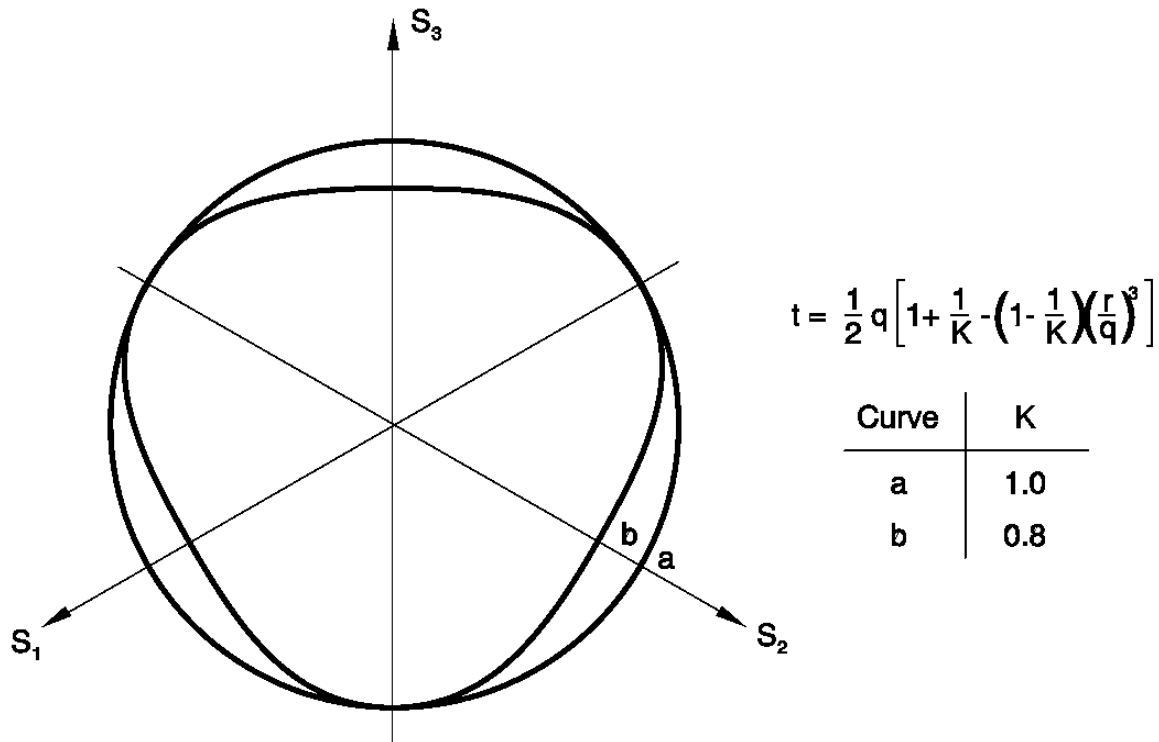


Figure 8. Typical Yield / Flow Surfaces in the Deviatoric Plane.



With this expression for the deviatoric stress measure, the Drucker-Prager failure surface is written as

$$F_s = t - p \tan \mathbf{b} - d = 0, \quad (22)$$

where  $\mathbf{b}(\mathbf{q}, f^a)$  is the material's angle of friction and  $d(\mathbf{q}, f^a)$  is the cohesion (see Figure 7). The cap yield surface has an elliptical shape with constant eccentricity in the meridional ( $p$ - $t$ ) plane and also includes dependence on the third stress invariant in the deviatoric plane. The cap surface hardens or softens as a function of the volumetric plastic strain: volumetric plastic compaction (when yielding on the cap) causes hardening, while volumetric plastic dilation (when yielding on the shear failure surface) causes softening. The cap yield surface is written as

$$F_c = \sqrt{(p - p_a)^2 + \left[ \frac{Rt}{\left(1 + \mathbf{a} - \frac{\mathbf{a}}{\cos \mathbf{b}}\right)} \right]^2} - R(d + p_a \tan \mathbf{b}) = 0, \quad (23)$$

where  $R(\mathbf{q}, f^a)$  is a material parameter that controls the shape of the cap,  $\mathbf{a}(\mathbf{q}, f^a)$  is a small number that is defined below, and  $p_a$  is an evolution parameter that represents the volumetric plastic strain driven hardening/softening. The hardening/softening law is a user-defined piecewise linear function relating the hydrostatic compression yield stress,  $p_b$  and the corresponding volumetric inelastic (plastic and/or creep) strain

$$p_b = p_b(\mathbf{e}_{vol}^{in}, \mathbf{q}, f^a) \text{ (Figure 9), where } \mathbf{e}_{vol}^{in} = \mathbf{e}_{vol}^{pl} + \mathbf{e}_{vol}^{cr}.$$

The evolution parameter,  $p_a$ , is defined as

$$p_a = \frac{p_b - Rd}{1 + R \tan \mathbf{b}} \quad (24)$$

The parameter  $\alpha$  is a small number (typically 0.01 to 0.05) used to define a smooth transition surface between the shear failure surface and the cap:

$$F_t = \sqrt{(p - p_a)^2 + \left[ t - \left(1 - \frac{\mathbf{a}}{\cos \mathbf{b}}\right)(d + p_a \tan \mathbf{b}) \right]^2} - \alpha(d + p_a \tan \mathbf{b}) = 0. \quad (25)$$

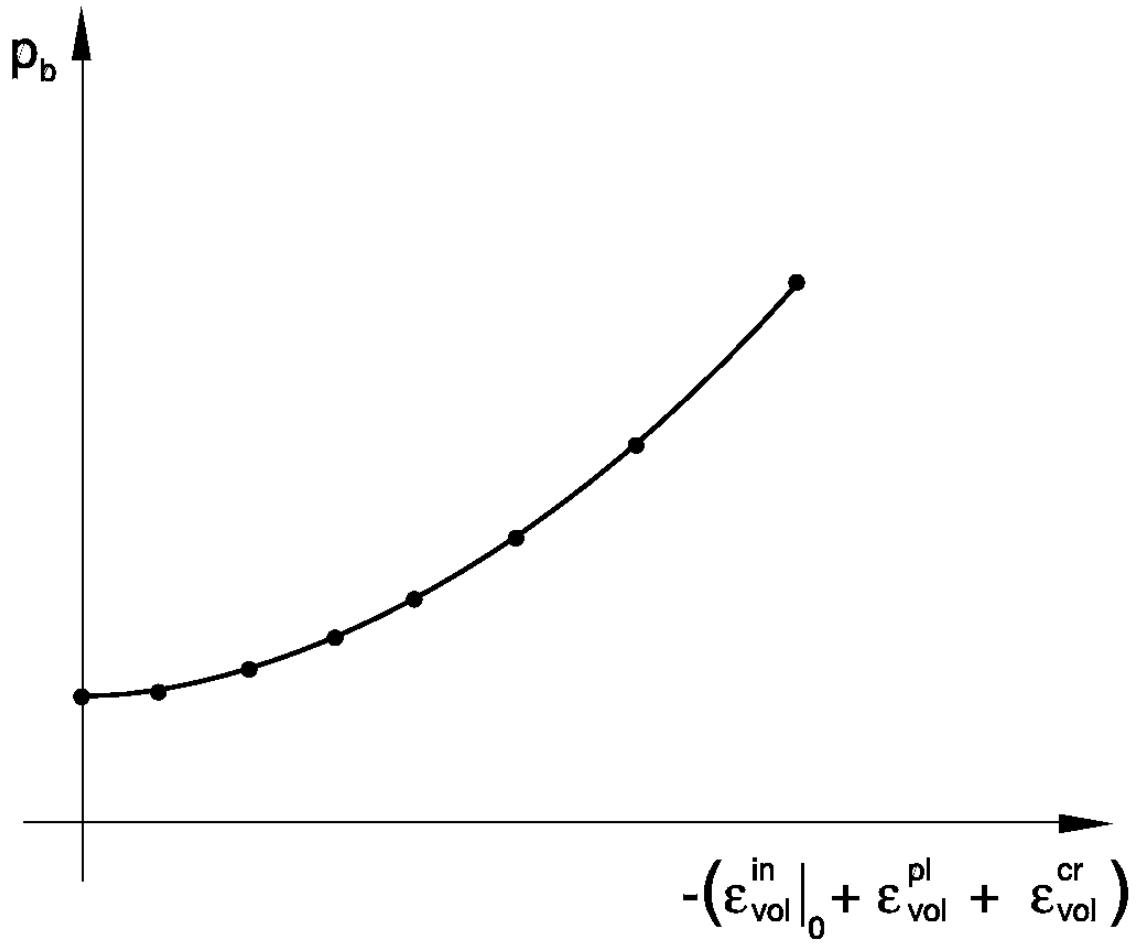


Figure 9. Typical Cap Hardening

Matching of experimental triaxial test data with the mathematical model parameters can be found in the ABAQUS manual.

Without experimental soil data for the foundation, the parameter values adopted to model the foundation were made through previous experience [Gong, 1993] and they are listed in Table 2.

Table 2. Parameters for the Drucker-Prager/Cap Plasticity Model

<i>Parameters</i>	<i>Soil Foundation</i>
<i>Density, <math>\rho</math> (kg / m<sup>3</sup>)</i>	2,000
<i>Modulus of Elasticity, <math>E</math> (Pa)</i>	10.0E+06
<i>Poisson's Ratio, <math>\nu</math></i>	0.2
<i>Material Cohesion, <math>c</math> (Pa)</i>	10.0E+03
<i>Material Angle of Friction, <math>\phi</math> (degrees)</i>	30.0
<i>Cap Eccentricity Parameter, <math>R</math></i>	0.1
<i>Initial Cap Yield Position, <math>e_{vol}^{pl}  _0</math></i>	0.001
<i>Transition Surface Radius Parameter, <math>a</math></i>	0.01

### ***Material Modeling of Waste***

The waste in the B-25 boxes has no definite geometric configuration and has no verifiable material properties. Since the radioactively contaminated materials placed into the boxes are not uniformly compacted, the void ratio of the waste in each of the boxes may vary from 30% to 50% [Phifer, Serrato, 2000] or more (new data even indicates a wider range of from 10% to 90%). The loosely disposed waste without clearly identifiable mechanical characteristics can be modeled as amorphous crushable materials. Some waste is compacted prior to placement within a B-25 box and the mechanical properties of the waste can be roughly determined.

The model for crushable foams is based on the critical state theory, which is widely accepted as a framework for describing porous materials such as soils and rocks. In the case of foams, the ability of the material to deform volumetrically (in compression) is enhanced by cell wall buckling processes. It is assumed that the resulting deformation is not recoverable instantaneously and can, thus, be idealized as being plastic for short duration events. In tension, on the other hand, cell walls break readily and as a result the tensile bearing capacity of foam is considerably smaller than its compressive strength.

The model uses a yield surface with an elliptical dependence of deviatoric stress on pressure stress. In the deviatoric plane yielding is assumed to depend on the third invariant of deviatoric stress. The evolution of the yield surface is controlled by the inelastic volume strain experienced by the material. The compactive inelastic strains produce hardening while dilatant inelastic volume strains lead to softening. Within the yield surface the material behaves linearly elastic.

The plastic behavior of the foam is regulated by a yield surface. In terms of the deviatoric stress measure,  $t$  as defined previously, the yield surface is formulated as

$$F = \left[ \left( \frac{p_t - p_c}{2} + p \right)^2 + \left( \frac{t}{M} \right)^2 \right]^{\frac{1}{2}} - \frac{p_c + p_t}{2} = 0, \quad (26)$$

where  $p_t = p_t(\mathbf{q}, f_i)$  is the strength of the material in hydrostatic tension,  $p_c(\mathbf{e}_{vol}^{pl}, \mathbf{q}, f_i)$  is the yield stress in hydrostatic compression,  $M(\mathbf{q}, f_i)$  is the slope of the critical state line in the  $p$ - $t$  plane. This yield surface is depicted in Figure 10.

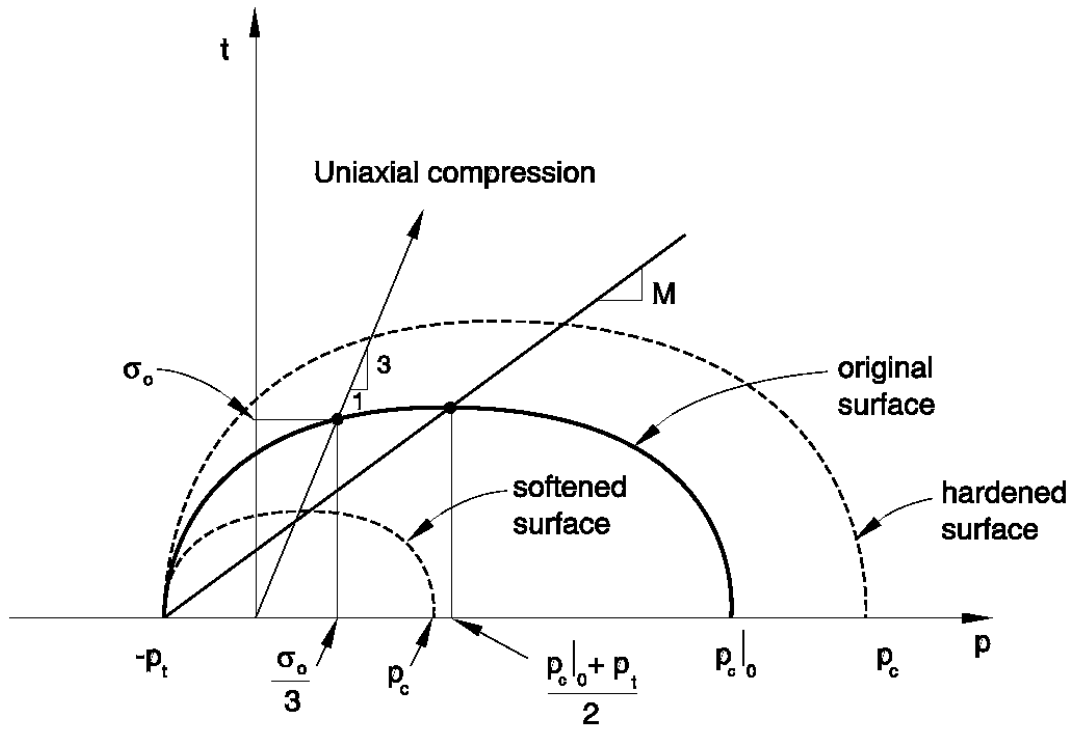


Figure 10. Yield Surfaces in the  $p$ - $t$  Plane for the Foam Model

$M$  is computed from the yield stress in uniaxial compression test as

$$M = \frac{s_0}{\sqrt{p_t p_{c|0} - \frac{1}{3} s_0 (p_t - p_{c|0}) - \frac{1}{9} s_0^2}}, \quad (27)$$

where  $\mathbf{s}_0(\mathbf{q}, f_i)$  is the initial yield stress in uniaxial compression (given as a positive value) and  $p_{c|0}$  is the initial value of  $p_c$ .

The yield criterion of Equation (26) defines an elliptic yield surface in the  $p$ - $t$  plane. The yield locus intersects the  $p$ -axis at points  $-p_t$  and  $p_c$ . In practice it assumes that  $p_t$  remains fixed throughout any plastic deformation process. By contrast, the compressive strength  $p_c$  evolves as a result of compaction or dilatation of the material (Figure 11).

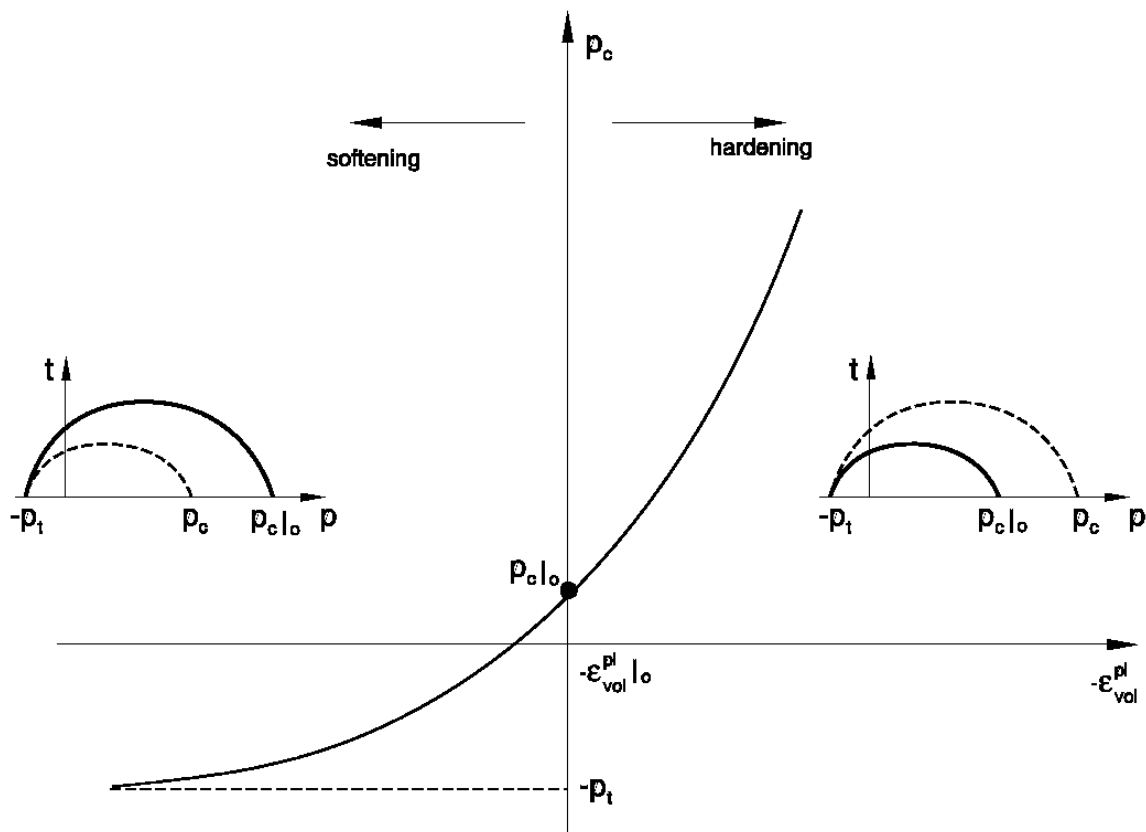


Figure 11. Typical Hardening / Softening Rule for the Foam Model

Without testing data for the waste disposed inside the B-25 boxes, two types of crushable foams are considered for the waste in alternate boxes. The parameters for this model can be modified, when the mechanical properties of the waste are available. The parameters for the two waste models are selected according to the mechanical properties of the Celotex™, which is a man-made material manufactured from sugar cane fibers.

In this analysis, the first waste constitutive model is based on the static properties of the Celotex™. Whereas, the second waste constitutive model is derived from the dynamic properties of the Celotex™ [Gong, 1999b, 2000], in which the stiffness is quadruple that of the static stiffness.

The parameters in the constitutive models of the waste are listed in Table 3

Table 3. Parameters for the Crushable Foam Plasticity Models of the Waste

<i>Parameters in the Model</i>	<i>Waste Type1</i>	<i>Waste Type 2</i>
<i>Density, <math>\rho</math> (kg / m<sup>3</sup>)</i>	200.308	240.308
<i>Modulus of Elasticity, E (Pa)</i>	2.54765E+08	1.01906E+09
<i>Poisson's Ratio, <math>\nu</math></i>	0.0	0.0
<i>Initial Yield Surface Position, <math>-\mathbf{e}_{vol}^{pl} _0 + \mathbf{e}_{vol}^{pl} ^+</math></i>	1.15	1.17
<i>Strength in Hydrostatic Tension, <math>p_b</math> (Pa)</i>	2.02327E+04	8.06549E+04
<i>Initial Yield Stress in Uniaxial Compression, <math>S_0</math> (Pa)</i>	5.10040E+05	2.04016E+06

The volumetric strain hardening curves of the two types of the waste models are plotted in Figure 12.

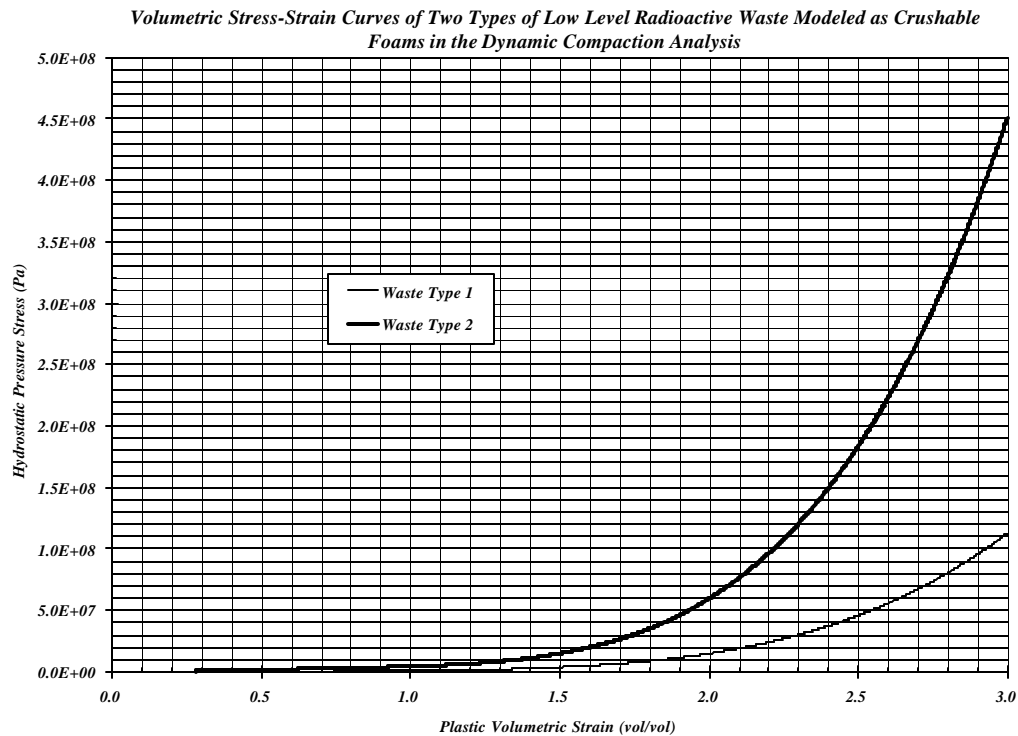


Figure 12. Volumetric Strain Hardening Curves for the Two Waste Models

The strain hardening strength of the type 2 waste is four times that of the type 1 waste. In this analysis, the distribution of waste in the B-25 boxes is shown in Table 4.

Table 4. Distribution of Waste in the B-25 Boxes in the Stack

<i>Position of the B-25 Box in the Stack</i>	<i>Type of the Waste in the Box</i>
<i>Top (Box 4: Top)</i>	<i>2</i>
<i>Next from the Top (Box 3: Middle Top)</i>	<i>1</i>
<i>Next from the Bottom (Box 2: Middle Bottom)</i>	<i>2</i>
<i>Bottom (Box 1: Bottom)</i>	<i>1</i>

## Applied Load

In the dynamic compaction the applied load is the drop of the impact weight. The weight is free falling from the height of 12.8 meter upon the top of the stack of four B-25 boxes [McMullin, 1994]. As the impact weight touches the top of the box-stack the dropping velocity is

$$V_{Impact\_weight} = \sqrt{2gh} = \sqrt{2 \times 9.805416 \text{ m/s}^2 \times 12.8 \text{ m}} = 15.843568 \text{ meter/second} \quad (28)$$

This velocity is applied as the initial condition for the impact weight when it drives into the stack of boxes. The initial kinetic energy is

$$\begin{aligned} \text{Kinetic Energy} = \text{Potential Energy} = Mgh &= 18,100 \text{ kg} \times 9.805416 \text{ m/s}^2 \times 12.8 \text{ m} \quad (29) \\ &= 2,271,719 \text{ N m} \end{aligned}$$

In Equations (28) and (29), the initial velocity and the corresponding kinetic energy are computed based upon an ideal free fall condition from 12.8 meter. In the field, the impact weight is hoisted up to the specified height by a crane. Then the impact weight is released from the crane tip to simulate a free fall. However the friction and other factors in the crane system will reduce the velocity of the falling impact weight. The best a crane can do is 90% of free fall. Usually the inefficiency of a crane is compensated by increasing the dropping height [McMullin, Dendler, 1994]

## Results

This is a nonlinear numerical calculation. The precision of the results depends on the computer platform and the modeling skills:

1. The size of the finite element mesh as compared to the strain gradient of the expected deformation of the boxes;
2. The choice of the “time increment” in the explicit time integration;
3. The precision of the computer;
4. The finite element modeling technique:
  - a. Correctness in complying with physical principles;
  - b. Understanding the limitation and capabilities of the finite element software;

Within the limit of our computational facilities, we obtained reasonably reliable solutions in this dynamic compaction analysis.

In this model, the total number of elements and nodal points are listed in Table 5.

Table 5. Number of Elements and Nodal Points in the Model

<i>Structural Member</i>	<i>Elements</i>	<i>Nodes</i>
<i>Four B-25 Boxes (3-D Shell Elements)</i>	<i>20,160</i>	<i>19,940</i>
<i>Waste in four B-25 Boxes (3-D Solid Elements)</i>	<i>280</i>	<i>576</i>
<i>Impact Weight (3-D Solid Elements)</i>	<i>1,536</i>	<i>2,451</i>
<i>Foundation (3-D Solid Elements)</i>	<i>1,536</i>	<i>2,023</i>
<i>Whole Mode</i>	<i>23,512</i>	<i>24,990</i>

### ***Determination of Time Increment in Explicit Integration***

In the numerical analysis with explicit time integration and reduced spatial integration (essentially it is a one-point integration) in each element, the numerical stability and accuracy of the calculation predominantly depend on the size of the time-increment. For a particular element the time increment can be chosen based upon the Courant-Friedrichs-Lewy stability criterion [Press, Flannery, Teukolsky and Vetterling, 1986]. This criterion is often called simply the Courant condition. Let  $|v|$  be the absolute value of the wave speed in the medium,  $\Delta x$  be the nominal linear size of the element and  $\Delta t$  be the time increment, then the Courant condition requires that

$$\frac{|v|\Delta t}{\Delta x} \leq 1 \quad (30)$$

The maximum time increment calculated from the above formula is 5.475E-06 seconds. The time increment determined for this analysis is 1.0E-06 seconds that is less than the time increment computed from the Courant condition. The Courant condition formulated in Equation (30) is for a system of differential equations with constant coefficients and fixed geometric configuration. In this dynamic compaction analysis both material properties and deformation configuration are highly nonlinear. The Courant condition is a reliable guide for choosing the proper time increment size. However, knowledge and experience in mathematics and mechanics will provide better understanding.

The numerical analysis is performed on the platform of an AIX version 4.3.3 computer. Both single precision and double precision computational options are applied. Obviously in a highly nonlinear analysis (with both geometric and constitutive nonlinearities), such as this analysis, double precision will provide more accurate numerical results. Only the results from the calculations with double precision are discussed in this report.



The impact weight drops from a height of 12.8 meter, which is the maximum impact height suggested for this dynamic compaction calculation [McMullin, 1994]. In the actual dynamic compaction practice, there is a layer of soil (about 2-meter) on the top of the B-25 box stacks. The layer of soil will certainly absorb a considerable amount of kinetic energy from the dropping impact weight. Limited by the available memory in the computer, the layer of soil is not included in the finite element model. The purpose of this analysis is to comprehend the mechanical behavior of the B-25 boxes and the waste inside under dynamic impact. The cover layer of soil may absorb a considerable amount of kinetic energy during the impact and reduce the dynamic force upon the boxes.

### ***Deformation Characteristics of the B-25 Boxes***

Under the dynamic impact, the stack of B-25 boxes deforms into the configuration as expected. As previously mentioned, the precision of the computer will influence the calculated results. Even though the finite element mesh is accurately modeled, the truncation errors and the solution method will slightly alter the final solution. Particularly in a nonlinear analysis, with millions of numerical operations in the computer, the accumulated truncation errors will carry the solution of the problem away from the true solution.

The B-25 boxes are manufactured with thin metal plates. A thin plate with considerable unsupported length along the direction of in-plane thrust will buckle into certain modal configuration as a function of the geometry and boundary conditions [Timoshenko and Gere, 1961, Timoshenko and Woinowsky-Krieger, 1959].

As a plate or shell buckles, it is bereft of its structural strength. In a numerical calculation, such as finite element analysis, the stiffness matrix comprises the strength of thousands of plate and shell elements. When a sufficient number of plate and shell elements buckle, the strength of the stiffness of the mechanical system will be seriously eroded and provide no resistance to the dynamic compaction. Then the calculation will be stopped.

In this analysis, the calculation stopped at 0.134111 seconds after the impact weight touched the top of the B-25 box stack. At this moment, various parts of the box walls of each of the four B-25 boxes are buckled.

The deformation of the stack of B-25 boxes is shown in Figure 13.

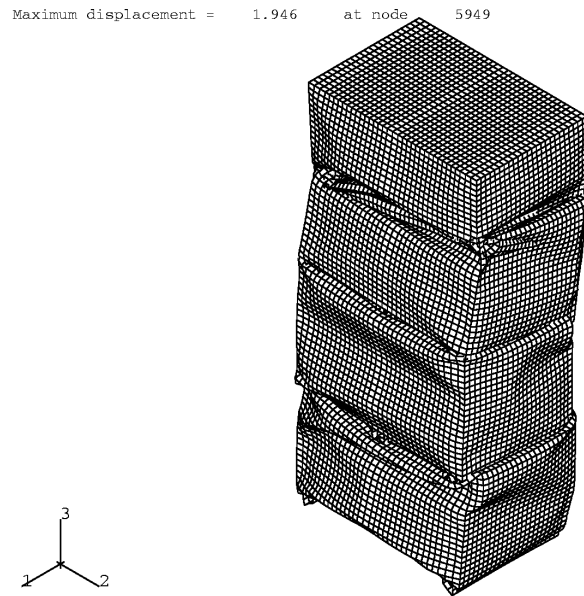


Figure 13. Deformation Configuration of a Stack of B-25 Boxes

The deformed configuration of each of the B-25 boxes demonstrates unique mechanical characteristics. The major mechanical influences are:

- (1) The dynamic impact source (relative location and potency);
- (2) The waste inside the B-25 boxes;
- (3) Mechanical properties of the materials;
- (4) The propagation of mechanical waves (wave speeds, wave reflection and refraction are function of material properties, geometric configuration and boundary conditions);
- (5) Mechanical interaction between contact surfaces (those surfaces that separate two mechanical bodies. Under compression, part of the surfaces will be in contact and may distort their configuration. However, these surfaces will not penetrate into each other. Without pressure, the surfaces belonging to different bodies will separate, i.e., the interfaces cannot sustain tension at all.)

The dynamic impact transmission and boundary conditions are different for each of the B-25 boxes in the stack. The deformation configuration of each individual box in the stack consequently possesses particular characteristics.

The deformation configuration of each individual box will demonstrate the path of dispersion of kinetic energy from the dynamic compaction in the mechanical system. Also the waste inside each of the boxes will definitely influence the dynamic process in the system.

The top B-25 box is at the source of dynamic impact power. The impact on the top box is from the direct impact of the dropping weight. Whereas, the dynamic impact forces in the underlying B-25 boxes in the stack are enormously influenced by the mechanical properties of the media in the paths of wave propagation and the boundary conditions.

The top box of the stack is inflicted by the direct impact from the dropping weight. The top lid of this box is pressed into a smooth flat surface. The sidewalls are buckled. The deformed configuration of the top B-25 box is shown in Figure 14. The bottom of this top box in contact with the top of the box beneath it is inward thrust, as depicted in Figure 15.

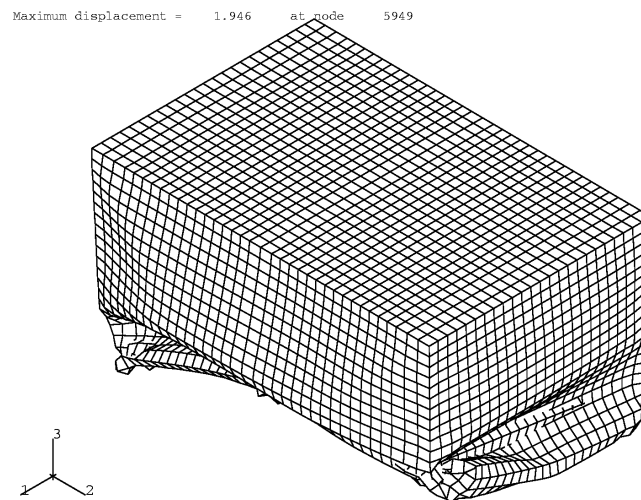


Figure 14. Top View of the Deformed B-25 Box (Box 4) at the Top of the Stack

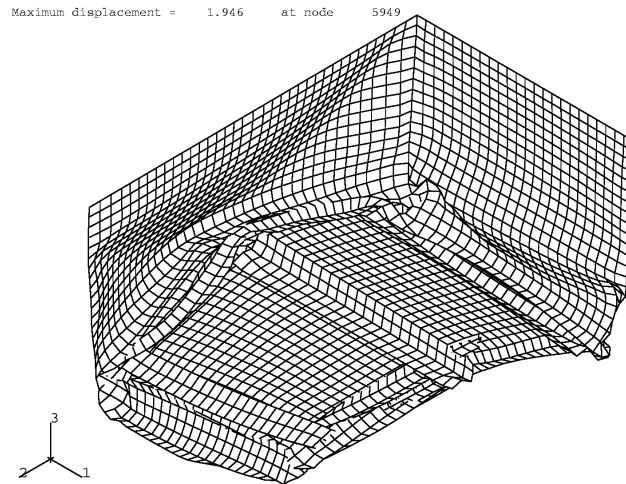


Figure 15. Bottom View of the Deformed B-25 Box (Box 4) at the Top of the Stack

The impulsive pressure waves from the dropping impact weight propagate through the top box (Box 4) walls. Both the impact weight and the lid of the top box (Box 4) are flat. The stress wave in the lid is very low. The stresses in the flat lid are mostly from the bending (rotation of the edge lines) of the intersectional edges of the side-walls and the lid.

In a completely different scenario, if a thick layer of unconsolidated soil is loaded on the top of the stack, as a bulldozer runs over the top of the soil, the lid of the top B-25 box will be caved into the box. The mass of the soil will thrust into the B-25 box.

The dropping of a relatively rigid block upon the top of the bare stack without a soil layer as a cushion resembles the mechanical condition of metal forming. The deformed flat top of the B-25 box (Box 4) is the consequence of the relatively incompressible waste inside and the flat contact surface of the weight block. The relatively incompressibility of the waste is not as a consequence of the material modeling. Rather it is a realistic kinematic situation. The dynamic impact impulse on the top of the B-25 box (Box 4) does not transmit through the thickness of the box lid. The dynamic impact waves propagate in the middle surfaces of the plates and shells of the boxes. The pressure over the contact interfaces between the waste and the interior surfaces of the box is negligibly small as compared with the dynamic impact. The structural instability of the box system occurred before the boxes crush over the waste. Physically, when the structural system reaches structural instability, further dynamic impact will smash the whole structure. The

mathematical model of the system will not carry out the calculations beyond the structural instability.

On the contrary, a layer of unconsolidated soil on top of the box stack is highly crushable. The pressure transmitted from the loading (on the top of the soil layer) to the interface of the bottom of the soil layer and the lid of the box is not uniformly distributed. The lid is supported by the plate walls on the four sides. The center of the lid deflects downward due to the pressure at the interface. High stresses along the edges of the box, eventually break integrity of the box and the lid falls into the box with the soil.

The waste inside the B-25 boxes can move freely during the dynamic compaction. The waste will damp off some kinetic energy from the impact loading. The mechanical waves generated from the dynamic impact will propagate through the metal walls of the boxes. During the dynamic compaction, the configuration of the interfaces between neighboring boxes will experience drastic deformation. The paths of wave propagation will be detoured and interrupted due to the opening and closing of the contact surfaces.

The contact surfaces between two adjacent B-25 boxes are the base of the three risers of the upper box and the lid of the box below. The contact of the risers and lid is relatively soft in the middle of the lid. Along the box edges the box walls resist the impact load transmitted through the risers. Therefore, in most cases the ends of the risers are crushed along the edges of the box, as shown in Figure 15.

The deformation of the B-25 box (Box 3) next from the top shows the effects of indirect transmission of the dynamic impact.

The top lid and the four sides of the B-25 box (Box 3) next from the top are severely buckled (Figure 16). However, the bottom plate of this box maintains relatively flat, and the middle riser undergoes little (or no) damage (Figure 17). Actually the bottom of the box (Box 3) next from the top box sinks into the lid of the top of the box (Box 2) immediately above the bottom box in the stack. The top four edges of the box (Box 2) next from the bottom box (Box 1) in the stack roll outward (Figure 18), such that the bottom of the box (Box 2) above squeezes right into the space.

The sidewalls of the box (Box 2) are all buckled. The bottom plate remains relatively flat (Figure 19).

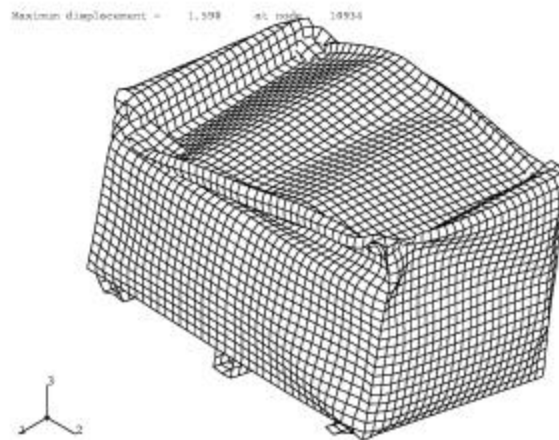


Figure 16. Top View of the Deformed B-25 Box (Box 3) Positioned Next from the Top of the Stack

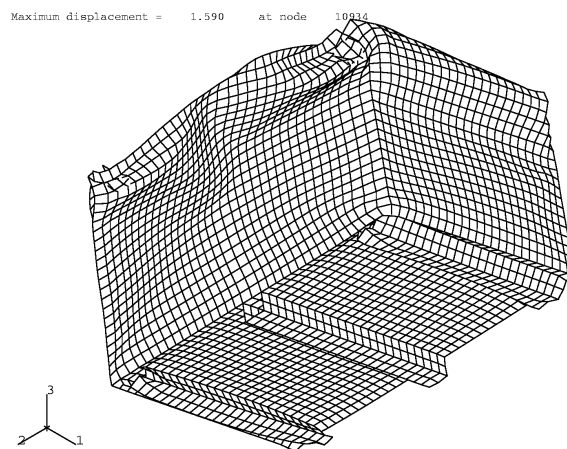


Figure 17. Bottom View of the Deformed B-25 Box (Box 3) Positioned Next from the Top of the Stack

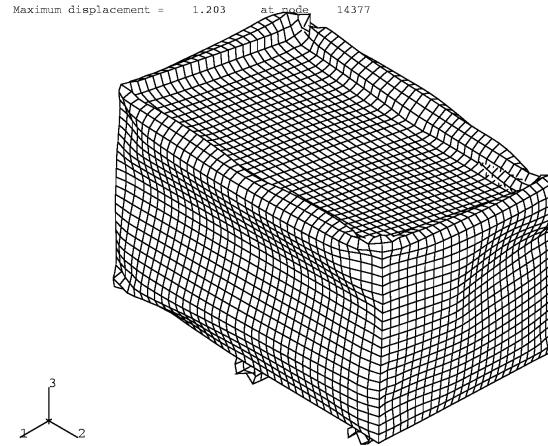


Figure 18. Top View of the Deformed B-25 Box (Box 2) Positioned Next from the Bottom of the Stack

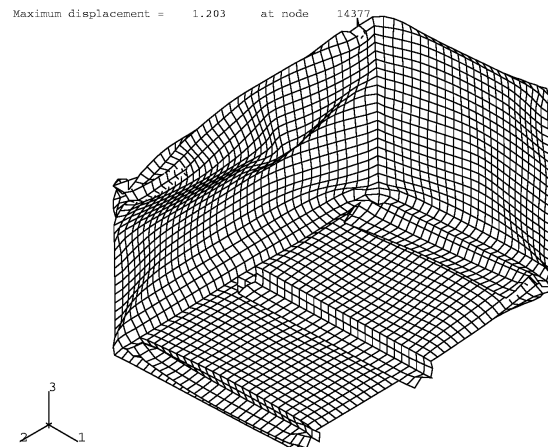


Figure 19. Bottom View of the Deformed B-25 Box (Box 2) Positioned Next from the Bottom of the Stack

This B-25 box (Box 2) that is the one above the bottom box (Box 1), is significantly influenced by the mechanical waves reflected from the ground foundation. If the ground foundation was solid and rigid, the reflected impact from the foundation would be considerably stronger and could inflict substantial damage on the boxes in the vicinity. Of course, the intensity of the mechanical impact gradually diminishes as the dynamic stress waves propagate through dissipative media.

The B-25 box (Box 1) at the bottom of the stack is in direct contact with the soil foundation (Figure 20). The dynamic impact reflected from the foundation punches the box from the bottom. The two risers along the edges of the bottom plate sink into the foundation as the compressive waves transmitted from the box walls. The bottom plate of the box deforms in the configuration of an arch (Figure 21).

The two deformed edge risers act as the abutments of the arch. The soil hump underneath the bottom plate is mechanically confined (Figure 22). The footprint of the stack of dynamically compacted B-25 boxes left a deep indentation in the foundation. The strength of the soil is a function of the confining pressure that is the hydrostatic pressure in this model. The combination of the interactions of propagation and reflection of the mechanical waves as well as the soil confinement effects the bending of the bottom plate intensifies.

During dynamic impact activity, ordinary engineering materials conspicuously exhibit energy dissipation; particularly the waste that is loosely composed of various substances is much more dissipative. However, in this analysis, no dissipation functions are specified for any of the structural members. The waste inside the boxes possesses complete freedom in all six degrees of freedom in each box. The deformation of the box has little effect on the configuration of the waste. This phenomenon will be displayed in Figures 23 and 24.

Allowing free movement of the waste in the B-25 boxes, the blocks of the waste sustain very little deformation during the dynamic compaction (Figures 23, 24)

The interior of the deformed B-25 boxes is shown in Figure 25.



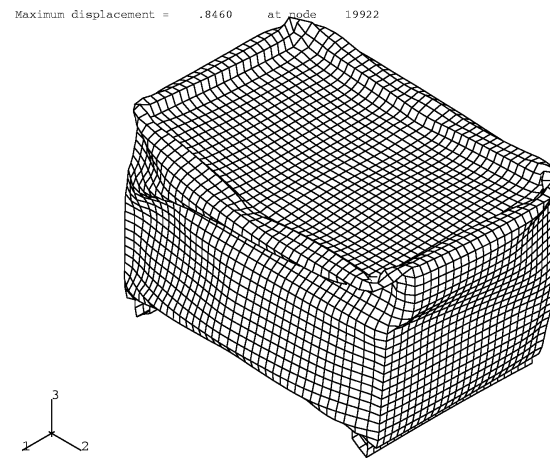


Figure 20. Top View of the Deformed Bottom B-25 Box (Box 1) in the Stack

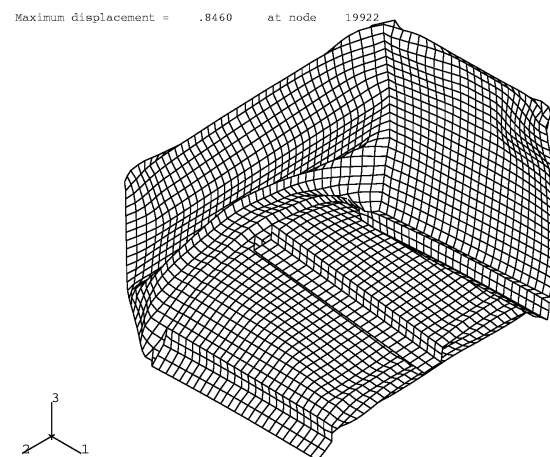


Figure 21. Bottom View of the Deformed Bottom B-25 Box (Box1) in the Stack

Maximum displacement = .5868 at node 2195

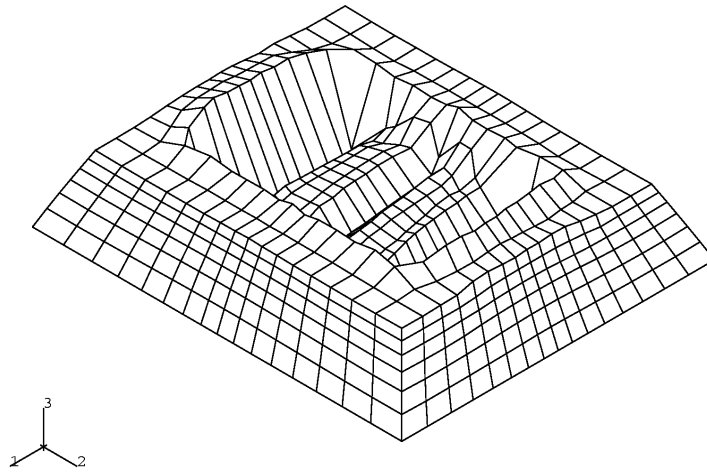


Figure 22. Deformed Soil Foundation

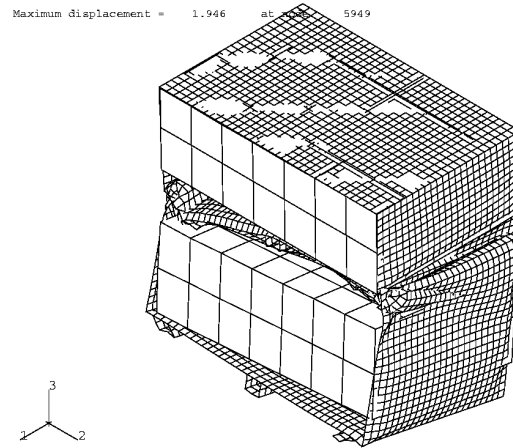


Figure 23. Top View of Two Deformed Top B-25 Boxes (Boxes 3 and 4) in the Stack with Waste Inside

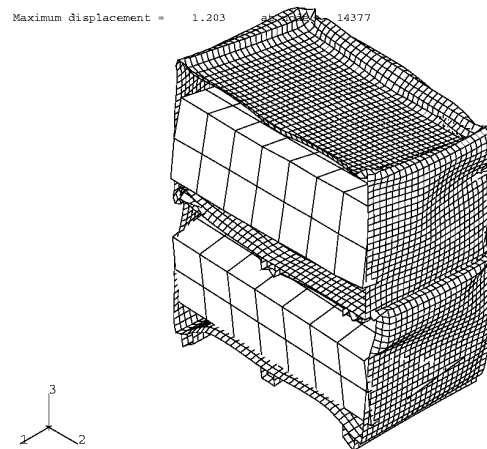


Figure 24. Top View of Two Deformed Bottom B-25 Boxes (Boxes 1 and 2) in the Stack with Waste Inside

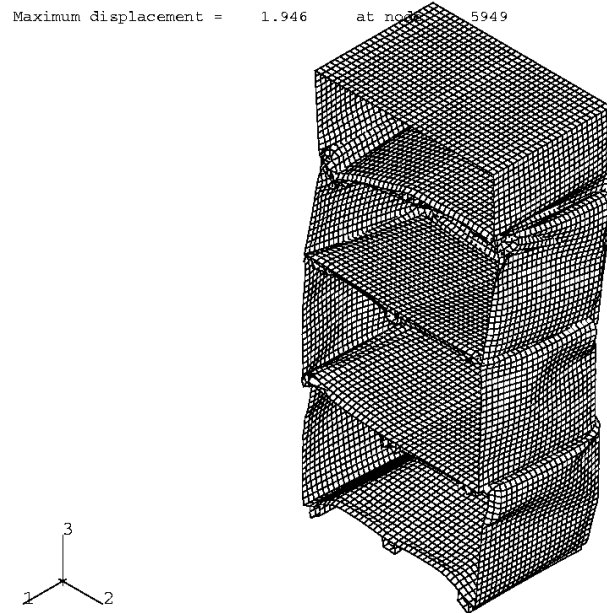


Figure 25. The Interior of the Stack of Deformed B-25 Boxes

### ***Time History of the Energies in the System***

In this dynamic system, the dropping impact weight (18,100 kg) from 12.8 meter is the source of the kinetic energy. As computed in Equation (29), the total amount of the kinetic energy is 2,271,719 N m (Newton-meter).

Both the impact weight and the B-25 boxes are made of steel. Particularly, the impact weight is relatively rigid. The clash of two metal components generates high speed mechanical waves. The propagation, reflection and refraction of the waves in the system produce vibrations with high frequencies.

A mechanical system with frequency dependent viscosity will dissipate energy through viscous damping mechanism. Since the actual viscous damping properties of the materials in the system under consideration are unknown, no viscosity is included in this mathematical model.

Also the impact from the clash is so intense, such that heat will be generated through high frequency vibrations and friction. Energy will certainly be dispersed in the thermal and friction processes. The friction coefficients between various mechanical components are virtually undefined. The conversion between mechanical energy and heat energy can make the calculations complicated. The significance of the energy exchange between thermal and mechanical interaction is overwhelmed by other more important factors in the system. Therefore, dissipation of energy through thermal and friction processes is neglected.

The impinging impact weight upon the top of the stack of B-25 boxes will certainly inflict massive deformation. The deformation of a mechanical system will consume energy. Part of the energy is recoverable and other types of energy are dissipated.

This system makes use of three types of materials, namely, steel (B-25 boxes and the impact weight), crushable foam (waste) and granular soil (foundation). During the massive deformation, a large portion of the materials underwent permanent distortion. The energy exhausted through the permanent deformation is dissipated and not recoverable. In this analysis, the dissipated energy is designated as the dissipated plastic energy. The time history of the three types of energies is plotted in Figure 26.

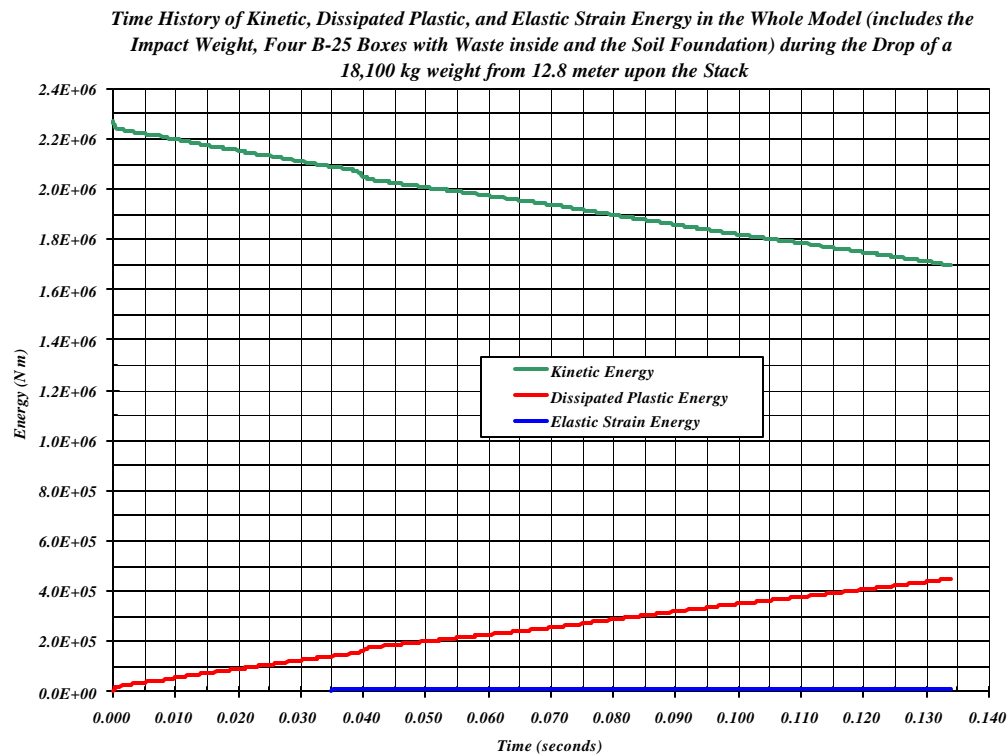


Figure 26. Time History of Kinetic Energy, Dissipated Plastic Energy and Elastic Strain Energy in the Whole Mechanical System

At the moment when the dropping impact weight touches the top the stack of the boxes, the total kinetic energy is in the impact weight with a magnitude of 2,271,719 N m. The impact upon the B-25 boxes releases a small amount of energy into the stack of boxes within 5.0E-04 seconds; the amount of the energy is 26,819 N m. Then, from time = 1.0E-03 to 3.9E-02 seconds the rate of energy transfer is almost constant. The constant decreasing rate is 4.495E+06 N m /second. From time = 3.9E-02 to 4.15E-02 seconds, the kinetic energy in the impact weight has a sudden drop at the rate of 13.0E+06 N m /second. After this sharp drop the driving kinetic energy maintains a constant decreasing rate of 3.684E+06 N m /second. The vanishing kinetic energy is partially stored as elastic strain energy in the mechanical system. Most part of the energy is dissipated during the plastic deformation of the system as shown in Figure 26.

The plastic energy dissipation occurs in all three types of materials, namely, steel (B-25 boxes), soil (foundation) and crushable foam (waste). The major energy dissipation takes place in the boxes and waste in this analysis. In Figure 27, the time history of the energies in the four B-25 boxes and the waste inside the boxes are displayed.

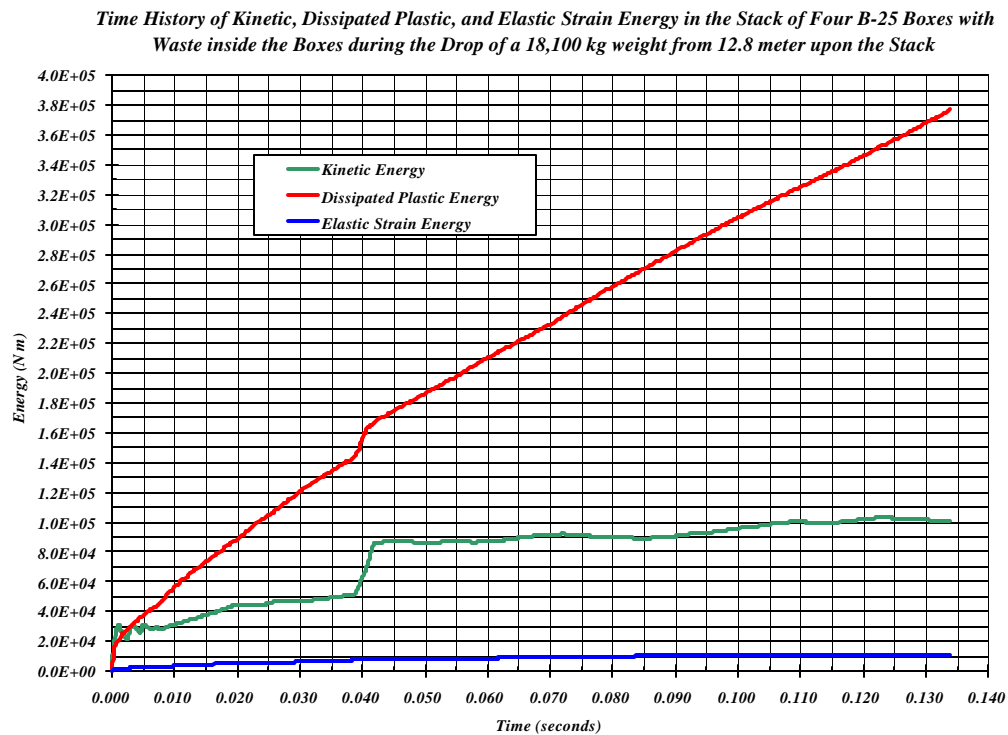


Figure 27. Time History of Kinetic Energy, Dissipated Plastic Energy and Elastic Strain Energy in the Stack of Four B-25 Boxes and Waste inside the Boxes

The sudden fluctuation of the energies in the boxes implies drastic mechanical change in the boxes during the time interval adjacent to 0.04 seconds. The boxes started deform as soon as the dynamic impact crashed into the top of the stack. The deformation of the boxes is mild until the time approaches 0.04 seconds. Significant distortion can be seen

in the boxes at time = 0.04 seconds. The snap-shots of the deformed second B-25 box (Box 3) from the top of the stack are depicted in Figures 28, 29, 30 and 31. Figure 28 shows the top view of the box (Box 3) in the first 0.04 seconds and Figure 29 displays the consecutive nine configurations of the box (Box 3) in the remaining 0.09 seconds. While Figures 30 and 31 depict the bottom views of the corresponding deformed box (Box 3) during the history of the dynamic impact.

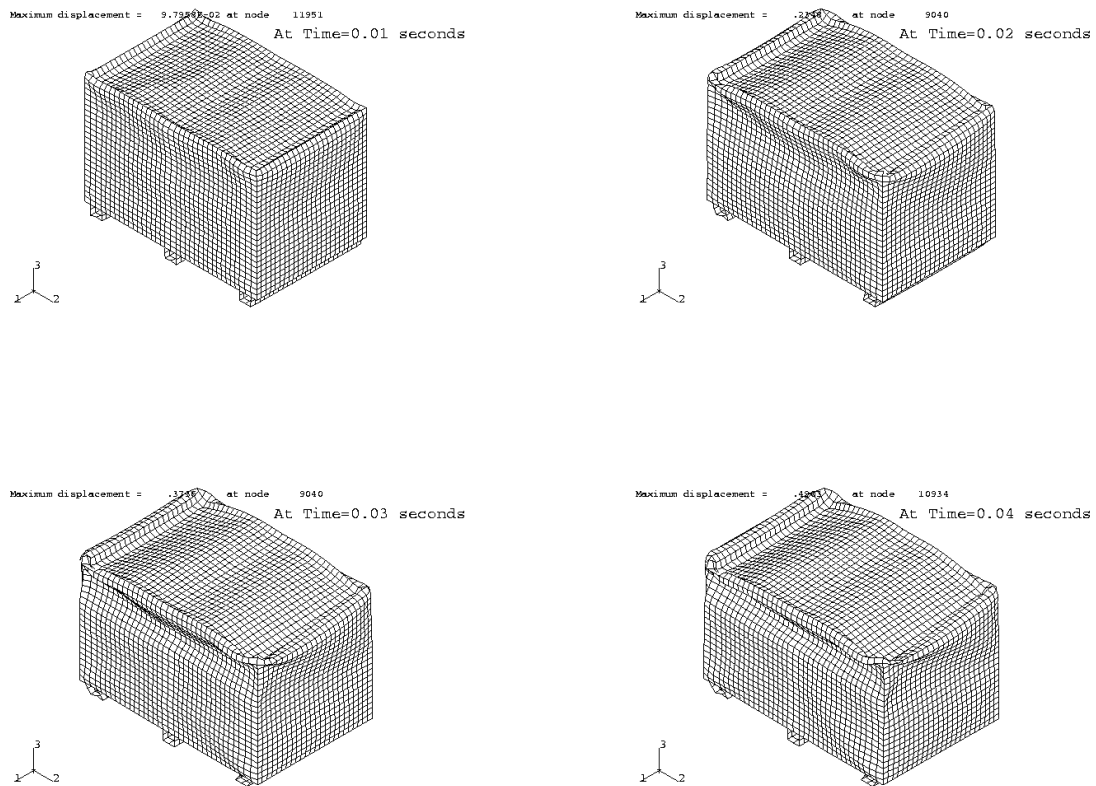


Figure 28. Top View of the Deformed B-25 Box (Box 3, second from the top of the stack) in the First 0.04 Seconds during the Dynamic Compaction

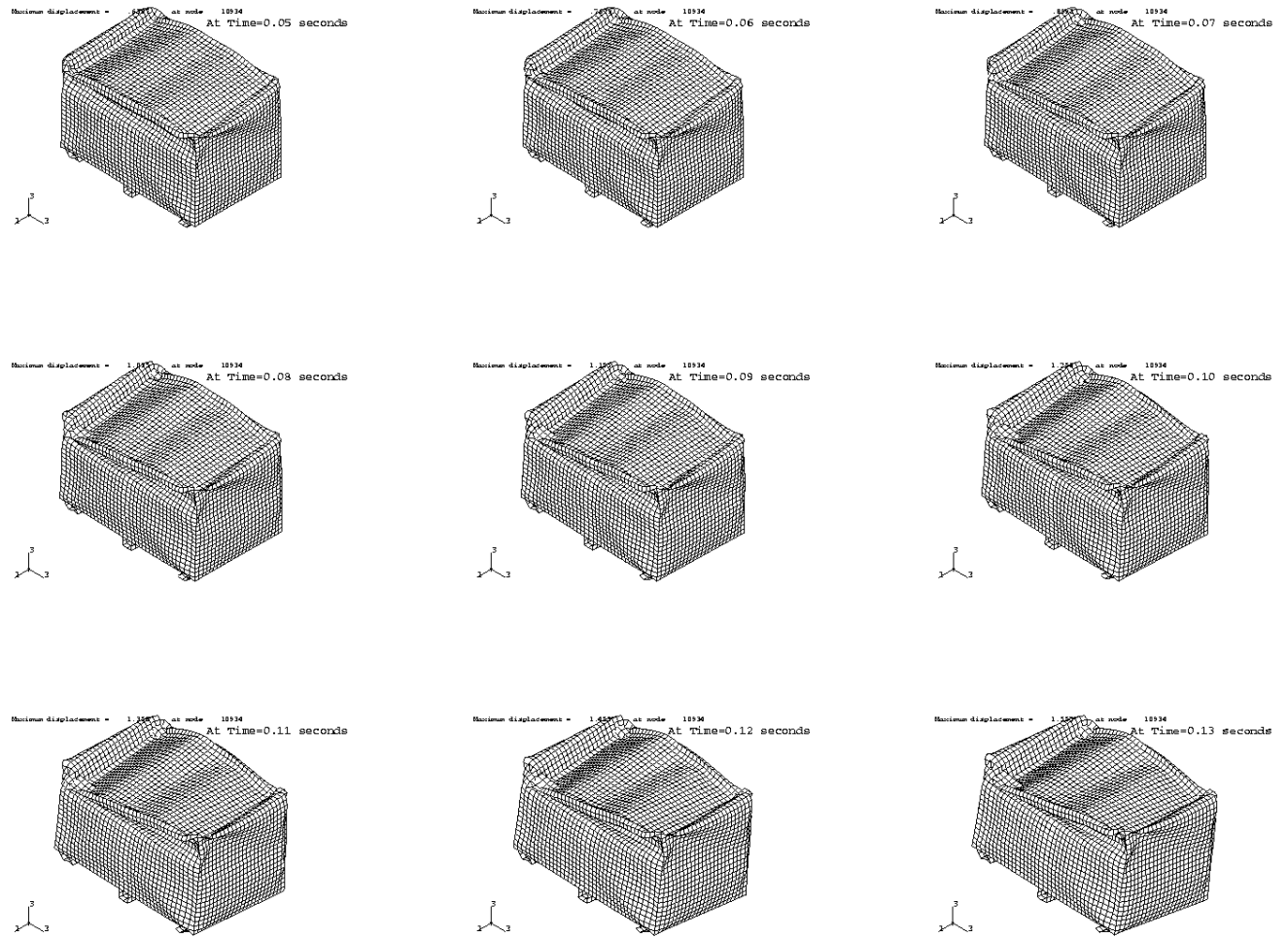


Figure 29. Top View of the Deformed B-25 Box (Box 3, second from the top of the stack) in the Last 0.09 Seconds during the Dynamic Compaction



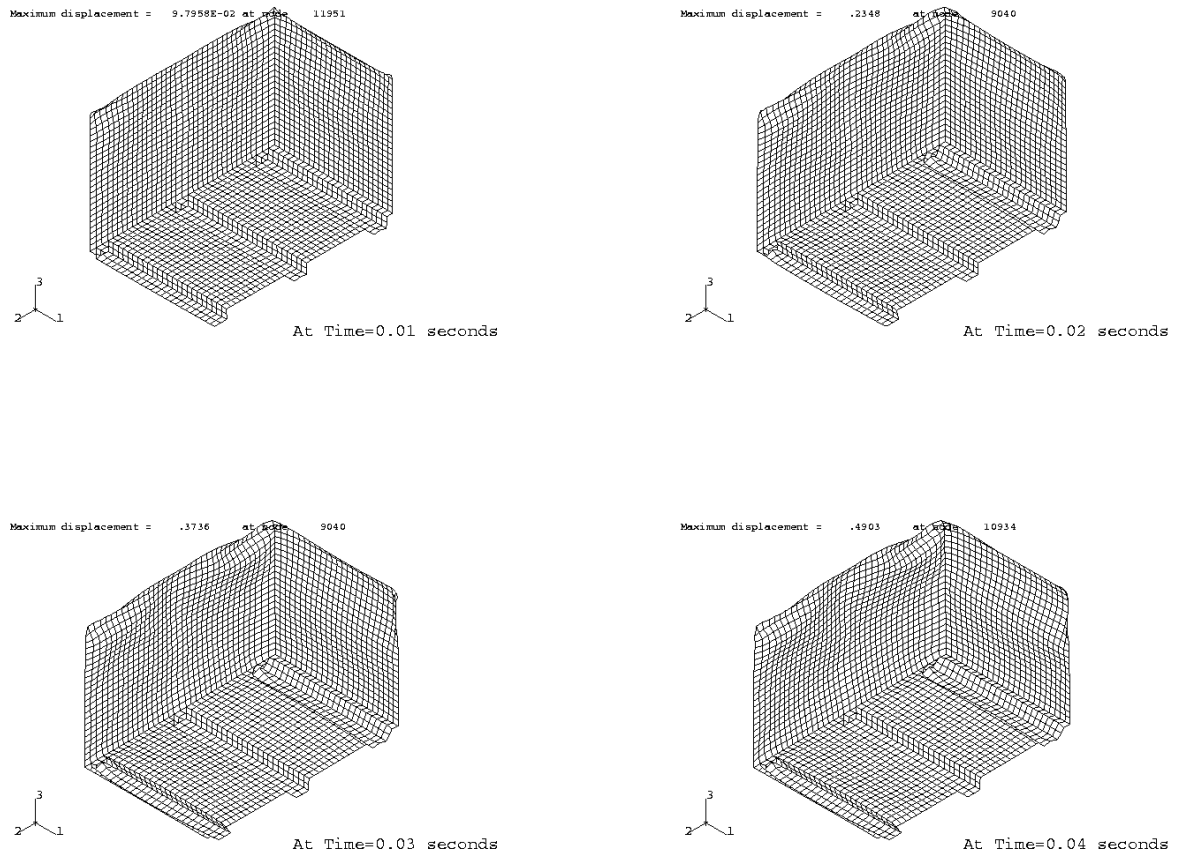


Figure 30. Bottom View of the Deformed B-25 Box (Box 3, second from the top of the stack) in the First 0.04 Seconds during the Dynamic Compaction

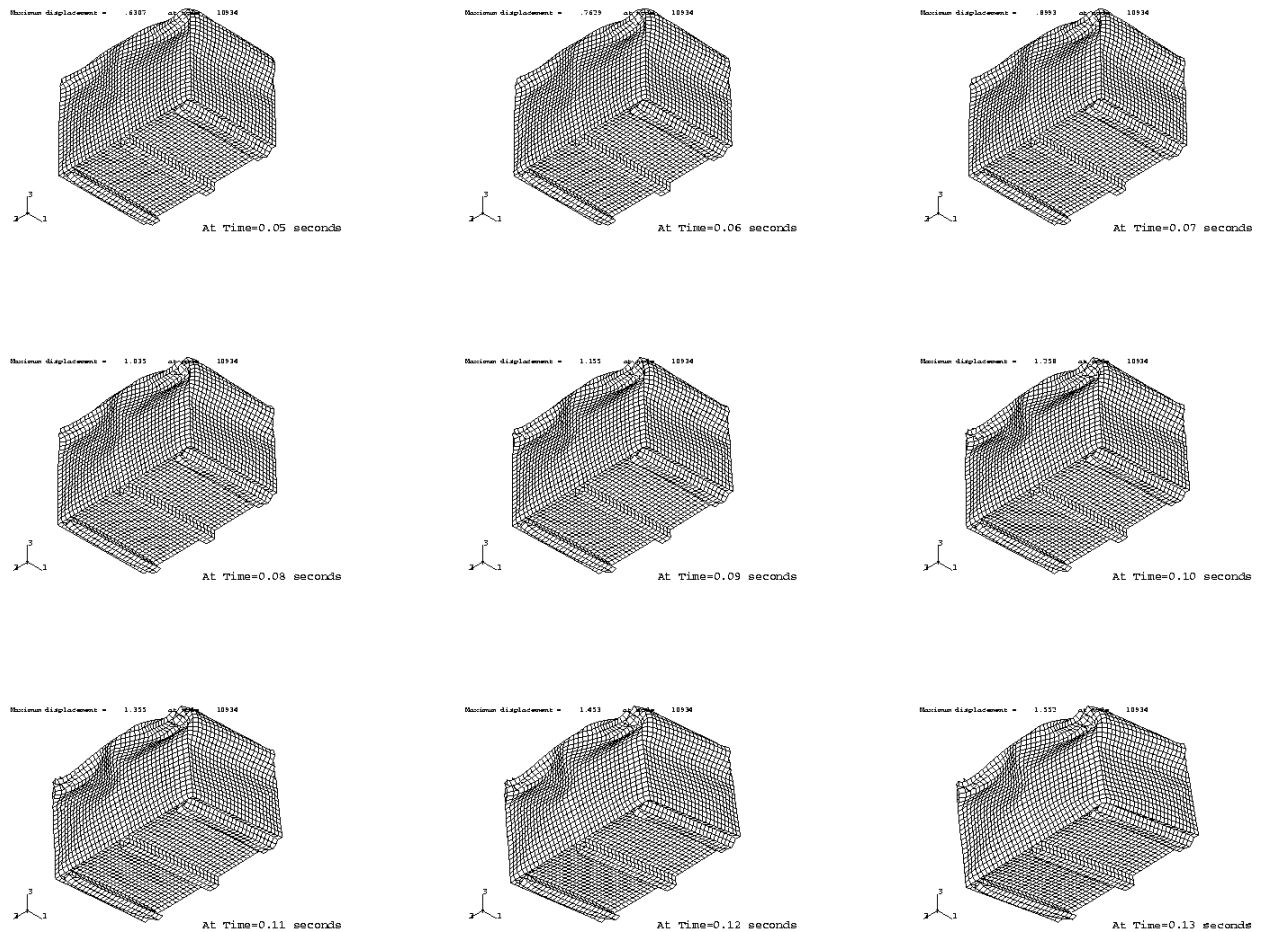


Figure 31. Bottom View of the Deformed B-25 Box (Box 3, second from the top of the stack) in the Last 0.09 Seconds during the Dynamic Compaction

The massive buckling process of the B-25 boxes initiates during the short time interval from 0.039 to 0.0415 seconds. The strength of the stack of boxes steadily deteriorates in the last 0.09 seconds until the mechanical system can no longer resist further dynamic impact. The residual kinetic energy of  $1.6976\text{E}+06$  N m is still dynamically significant.

As the material strength rapidly deteriorates in the numerical calculation, the imposing kinetic energy upon the mechanical system will induce a deformation speed, which is faster than the velocity of wave propagation in the system. This condition generates numerical instability and the computation process stops.

In the actual physical situation, the intrinsic structural instability will induce drastic deformation in the system. Through multiple kinematic processes the deformed mechanical system may approach a final stable configuration. This will involve

extensive computational operations to bridge the gap of mechanical instability. If the waste inside boxes does not have sufficient structural strength, the system may collapse after massive element buckling occurs.

The main interest in this analysis is to examine the mechanical behaviors of the stacked B-25 boxes with partially filled waste during dynamic compaction. The essence of the mathematical model of the boxes is physically accurate. Nevertheless a few mechanically important attributes are eliminated. These factors are important to the actual dynamic compaction results, but those contribute little for the understanding of the mechanical behavior of the B-25 boxes. Including all the physical components will heavily burden the computational process. In reality the characteristics of those mechanical factors are random and cannot be accurately modeled. The few factors are:

- The soil layer on top of the stack;
- The surrounding stacks of B-25 boxes;
- The circular impact weight has a diameter of 8-foot that will certainly touch more than one stack when it drops upon a group of stacks of boxes;
- The randomness of relative position between boxes in the stack.

The loosely deposited soil layer has high void ratio and air containment. The density of the soil may be increased from 90 pcf to 120 pcf in the first drop of the impact weight. The thickness of the soil layer may be reduced by 25%. A significant amount of energy will be dissipated in this soil compaction process.

The surrounding stacks of boxes certainly provide appreciable confinement to the central stack that is under dynamic compaction. The amount of confinement cannot be quantified and is randomly distributed in nature.

The dynamic impact load from the 8-foot diameter impact weight and being transmitted through a layer of soil will be distributed over an area larger than the 8-foot circle on the stacks of boxes. The dynamic impact load distribution over the stacks cannot be pre-determined.

Structural instabilities in a mechanical system are usually initiated by geometric imperfection. Aligning the four B-25 boxes in perfect tidiness is almost impossible in practice.

Consequently, during the dynamic compaction, a particular stack of boxes may carry only a small portion of the total dynamic load. With multiple impact weight drops, the stack of boxes may be compressed but may not be smashed. Since the dynamic impact load distributed on the particular stack in each of the multiple drops may be considerably small.

In this analysis, the entire dynamic impact load is directly applied on the top of the stack of boxes. The geometric configuration of the stack of boxes is precisely modeled.

Initially, in the calculation, the stack of boxes has no “geometric imperfection” until sufficient numerical “truncation errors” and other inherited finite element analysis approximations (especially the “hour glass” phenomenon caused by reduced element integration in explicit procedure) accumulated in the system. Excessive kinetic energy leads the precisely modeled stack of boxes to early buckling and collapse. However, the analysis serves the purpose for understanding of the mechanical behavior of the B-25 boxes and the feasibility of performing 3-D finite element analysis of the subsidence in the engineered trench.

### ***Pseudo-Engineering Stress Strain Curve in the Dynamic Compaction***

The mechanical influence to the subsidence of the closure cap from the dynamic compaction of the B-25 boxes in the engineered trench can be numerically modeled and analyzed. However, if sufficient details of hundreds of B-25 boxes are modeled in the engineered trench, the number of elements of the finite element model (including soil foundation and clay cap system) will be well over a few millions. A finite element model with a million elements is difficult (if not impossible) to perform computation on the computers available for use at SRS.

The approximate mechanical properties of the B-25 boxes in the trench may be estimated from the pseudo-engineering stress strain relations.

Without including the mechanical details, over the bottom face of the impact weight, the displacement and acceleration ( and deceleration) are saved during the dynamic analysis.

Let

- $S$  = Pseudo-engineering stress,
- $a_3$  = The vertical component of deceleration at the bottom of the impact weight,
- $A$  = Area of the contact surface between the bottom of the impact weight and the top lid surface of the top B-25 box in the stack,
- $M$  = Mass of the impact weight,
- $u$  = The vertical component of displacement at the bottom of the impact weight,
- $H$  = The undeformed height of the stack of four B-25 boxes,
- $\epsilon$  = Pseudo-engineering strain.

Then, the pseudo-engineering stress can be computed as

$$S = \frac{a_3 \times M}{A} \quad (31)$$

In the numerical calculation the deceleration is computed as the average of the vertical component of the acceleration over 143 nodes over the bottom of the impact weight.

The pseudo-engineering strain can be computed as

$$\mathbf{e} = \frac{u}{H} \quad (32)$$

The displacement in Equation (32) is the average value of the vertical component of the displacement of 143 nodes on the bottom of the impact weight.

The “complete” pseudo-stress strain curve is plotted in Figure 32.

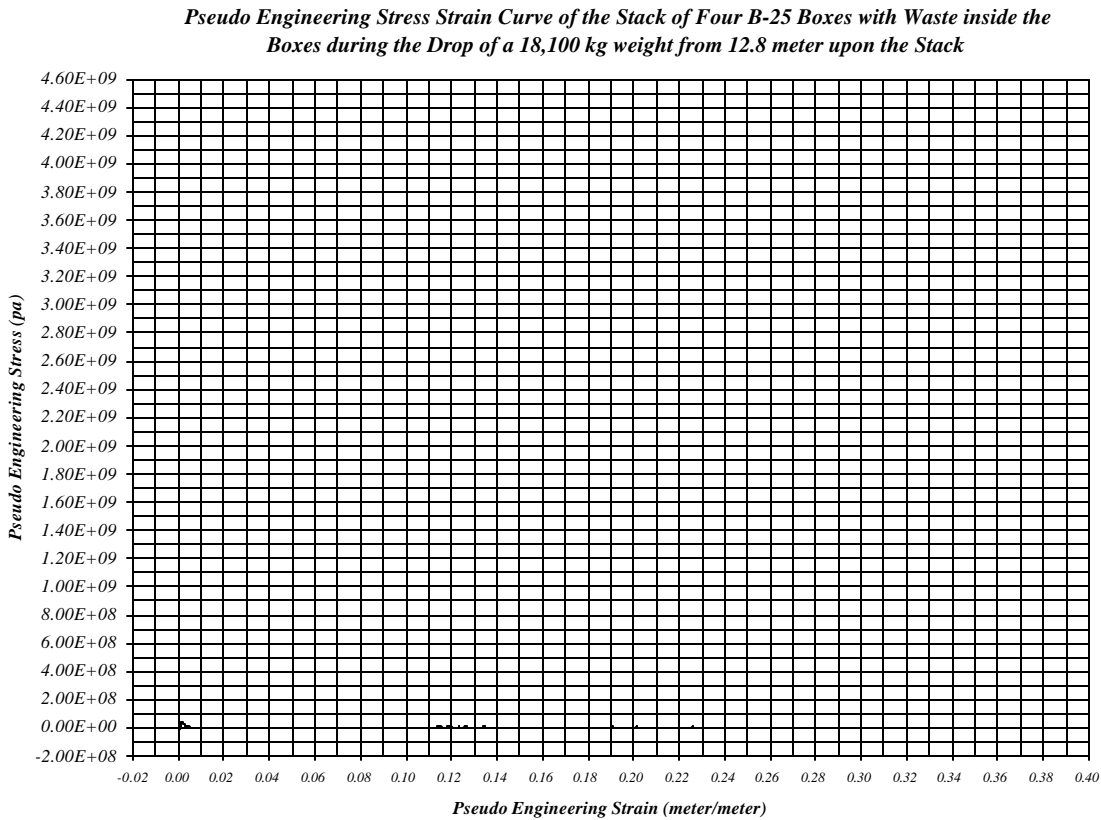


Figure 32. The Complete Pseudo-Engineering Stress Strain Curve for the Dynamic Compaction of a Stack of Four B-25 Boxes with Waste Inside the Boxes

The pseudo-engineering stress from the initial dynamic impact dominates the stress strain plot.

The four B-25 boxes as well as the impact weight and the soil foundation are precisely aligned in the mathematical modeling process; consequently before any forceful disturbance the mechanical system is in perfect symmetry.

As the impact weight touches the top of the stack, the whole system behaves like a rigid body. The initial pseudo-engineering stress reaches 4.5477E+09 Pa that is much higher than the ultimate tensile strength (3.85624E+08 Pa) of the steel used for the B-25 boxes.

The dilatational wave velocity in the B-25 boxes is 5,839 meter/second. The total height of the stack of the four boxes is 5.2249 meter (that includes the thickness of the steel plates and the precision of the modeling code). It will take  $8.9487\text{E-}04$  seconds for the dilatational wave to travel from the top of the stack to the bottom of the bottom box without other interference. Consequently at the initial instant (that is less than  $1.0\text{E-}06$  seconds), before the waves reflect from various components and boundaries of the mechanical system, the structure has no response. The system behaves like a rigid body at this moment.

However, at time =  $1.0\text{E-}06$  seconds (the time increment chosen for the numerical calculation), the pseudo-engineering stress at the interface of the impact weight and the top of the stack turns to be tensile stress ( $1.5487\text{E+}07$  Pa) instead of compression. That implies the mechanical system has little resistance to the falling impact weight at this moment. Of course, in the time interval between 0.0 to  $1.0\text{E-}06$  seconds, a lot of wave propagation and reflection in the system are in progress. The time increment of  $1.0\text{E-}06$  seconds is already much less than the value ( $5.475\text{E-}06$  seconds) established by Equation (30). Further reduction of the time increment (without corresponding increase of the finite element mesh density) will not improve the accuracy of the solution.

Limited by the memory capacity of the computing device, the time history of the displacement, velocity and acceleration vectors are saved at every  $5.0\text{E-}04$  seconds that gives 270 data points for each curve. Without recording every data point in a high frequency dynamic analysis like this one, the true maximum and minimum responses of the mechanical system are lost.

At time =  $5.0\text{E-}04$  seconds, the pseudo-engineering stress (compression) reaches  $4.0817\text{E+}07$  Pa that is the stress descended from the peak stress at previous moment that is not recorded. Apparently, under high pressure many structural components in the boxes are buckled. The stress continuously declines until time =  $2.0\text{E-}03$  seconds and the corresponding pseudo stress and strain are  $4.2\text{E+}05$  Pa and  $6.0225\text{E-}03$  respectively. The multiple buckling process in the system weakens the strength of the boxes. Within the time interval from  $2.0\text{E-}03$  to  $3.85\text{E-}02$  seconds the strain is accumulated to 0.1133 (i.e., 11.33%) and the pseudo-engineering stress fluctuates between  $-1.3403\text{E+}06$  and  $+2.0996\text{E+}06$  Pa as shown in the truncated stress strain curve depicted in Figure 33.

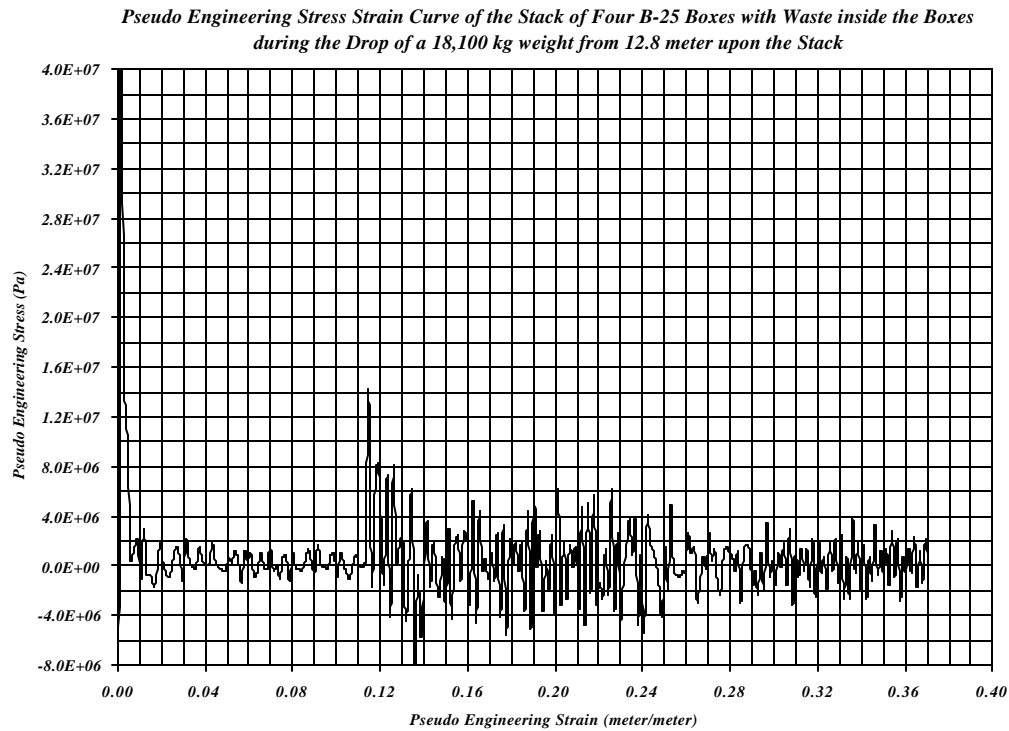


Figure 33. The Truncated Pseudo-Engineering Stress Strain Curve for the Dynamic Compaction of a Stack of Four B-25 Boxes with Waste Inside the Boxes

At time =  $3.9\text{E-}02$  seconds, the pseudo-engineering stress suddenly increases to  $1.4247\text{E}+07$  Pa and the corresponding strain is 0.1147 (or 11.47%). This phenomenon implies that the initial massive buckling reshaped the configuration of the mechanical system into a different structurally stable geometry. The strength of the system is partially recovered. Nevertheless, the remaining kinetic energy ( $2.0709$  N m) at this moment is still considerably powerful and imposes second massive buckling upon the mechanical system. The manifest deformation configurations of one of the four boxes are depicted in Figures 28, 29, 30, and 31. After this devastating second crash the strength of the system gradually deteriorates. The pseudo-engineering stress varies between  $-7.8135\text{E}+06$  and  $+8.3152\text{E}+06$  Pa and eventually decays to  $-1.3136$  and  $+2.1214\text{E}+06$  by the end of the calculation. The calculation stopped due to the remaining kinetic energy in the impact weight overpowers the strength of the B-25 boxes.

This mechanical behavior of the B-25-box system is strikingly similar to the stress-strain relations of the cellular solids [Gibson and Ashby, 1999]. It implies that the assembly of hundreds of stacks of B-25 boxes can be modeled as cellular solids. The initial elastic stress in the stress-strain curve indicates that the steel walls of the B-25 boxes carry the initial impact. A few of the steel walls buckled and the boxes consolidated under the still powerful impact. Then further buckling occurs in the box walls that causes high stress in the time interval from 0.03 to 0.04 seconds.

### ***Will Finer Finite Element Mesh Improve the Dynamic Compaction Results?***

In theory, the calculation of an initial value and boundary value problem through the numerical method of finite element analysis modeling will asymptotically approach the exact solution, if the number of elements increases as the size of the elements decreases. However, in reality, the degree of precision of a computer is limited, as the number of elements increases the number of numerical calculation operations increases accordingly. Each numerical operation will contribute truncation error to the numerical system. Particularly, in a nonlinear analysis, the iteration process heavily depends on the precision of the computer. Without sufficient precision, increasing number of elements will not furnish a better solution to the problem.

Particularly, in an analysis with both material and geometrical nonlinearities, the result calculated in the previous step will be used as initial condition for the present step. A slight alteration in each integration step will deviate the solution to a very different configuration after a million iterations. For a perfectly linear problem reducing finite element mesh size will improve the results of the solution.

Nevertheless, a refined finite element analysis model with the shell elements increased to quadruple of the present model was constructed. The number of elements and the number of nodes are shown in Table 6. With the same loading, initial conditions and boundary conditions, the calculations take much longer time. The numerical calculation with the time increment determined by the code stopped (at 0.1297 seconds) even before the previous case (0.13411 seconds). As discussed previously, Equation (30), the selection of time increment in each step is based on the time for dilatational wave travelling through an element in the region of calculation. However, when the time increment is reduced from the code-determined (average) value of 2.714275E-06 seconds to a fixed time increment of 1.0E-06 seconds, the calculation continued much longer (0.1564 seconds) before reaching instability.

Table 6. Number of Elements and Nodal Points in the Refined Model

<b><i>Structural Member</i></b>	<b><i>Elements</i></b>	<b><i>Nodes</i></b>
<i>Four B-25 Boxes (3-D Shell Elements)</i>	87,800	87,352
<i>Waste in four B-25 Boxes (3-D Solid Elements)</i>	280	576
<i>Impact Weight (3-D Solid Elements)</i>	1,536	2,451
<i>Foundation (3-D Solid Elements)</i>	1,536	2,023
<i>Whole Mode</i>	91,152	92,402

The computation time utilized for the completion of each of the three models on the Central Processing Unit (CPU) of an IBM AIX version 4.31 machine is listed in Table 7.



Table 7. Time Increments and CPU Times for Three Computational Models

<i>Model</i>	<i>Elements</i>	<i>Nodes</i>	<i>Total Time Completed Before Instability Occurred (seconds)</i>	<i>Time Increment (seconds)</i>	<i>CPU Time (seconds)</i>
<i>Coarse</i>	23,512	24,990	0.1341	1.000000E-06	75,539
<i>Refined</i>	91,152	92,402	0.1298	2.714275E-06	102,701
<i>Refined</i>	91,152	92,402	0.1564	1.000000E-06	339,611

The CPU times listed in Table 7 also reflect the cost for each calculation. The CPU time utilized for each second of completed calculation of the three models can be computed as  $5.63304\text{E}+5$ ,  $7.81225\text{E}+05$  and  $21.71426\text{E}+05$ , respectively.

The refined finite element mesh of the four boxes is shown in Figure 34 that can be compared with Figure 5.

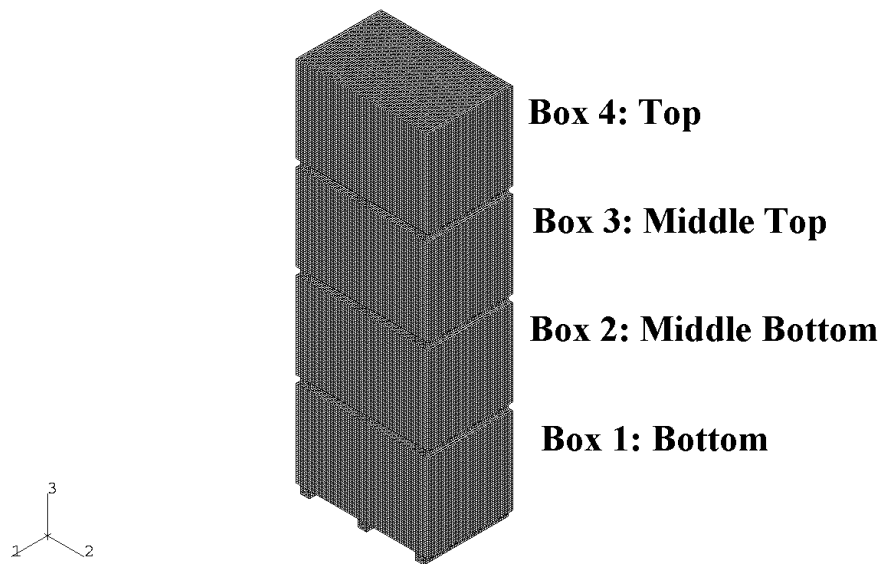


Figure 34. Isometric Top View of a Finite Element Analysis Model with Refined Mesh of a Stack of Four B-25 Boxes

The finite element analysis model with refined mesh of one B-25 Box is shown in Figure 35 for comparison with Figure 2.

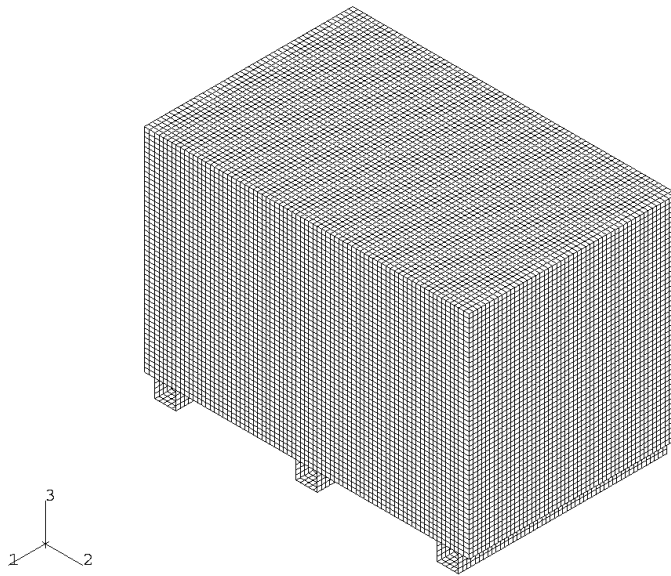


Figure 35. Isometric Top View of a Finite Element Analysis Model with Refined Mesh of one B-25 Box

The detail of the deformed configuration of the B-25 boxes with refined finite element mesh is certainly different from that with coarse mesh. The deformed configuration of the stack of four B-25 boxes, calculated with code-determined time increment, is depicted in Figure 36.

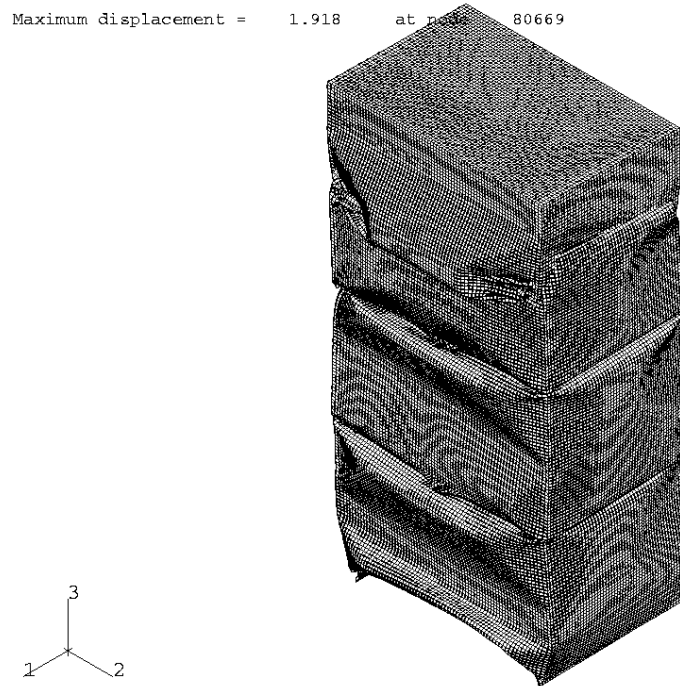


Figure 36. Isometric Top View of the Deformed Stack of Four B-25 Boxes modeled with Refined Finite Element Mesh and Calculated with Code-determined Time Increment

The top two boxes (Boxes 3 and 4) are mutually wrapped around together. The individual deformed configuration will show details of the deformation. The top and bottom views of the B-25 box (Box 4) at the top of the stack are shown in Figures 37 and 38.

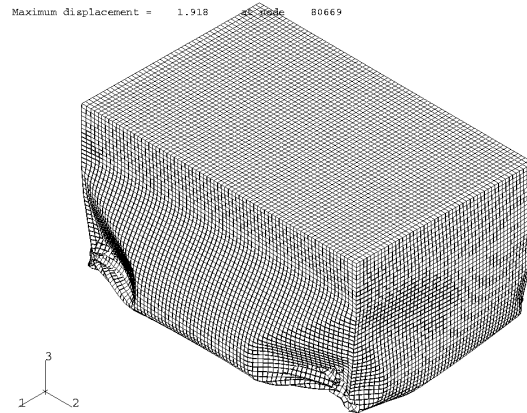


Figure 37. Isometric Top View of the Deformed B-25 Box (Box 4) on the Top of the Stack modeled with Refined Finite Element Mesh and Calculated with Code-determined Time Increment

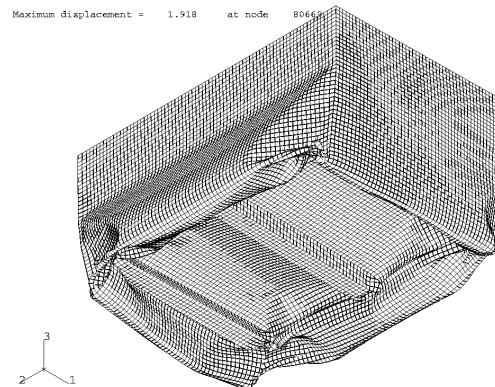


Figure 38. Isometric Bottom View of the Deformed B-25 Box (Box 4) on the Top of the Stack modeled with Refined Finite Element Mesh and Calculated with Code-determined Time Increment

The deformed configuration of the B-25 box (Box 3) second from the top of the stack is depicted in Figures 39 and 40.

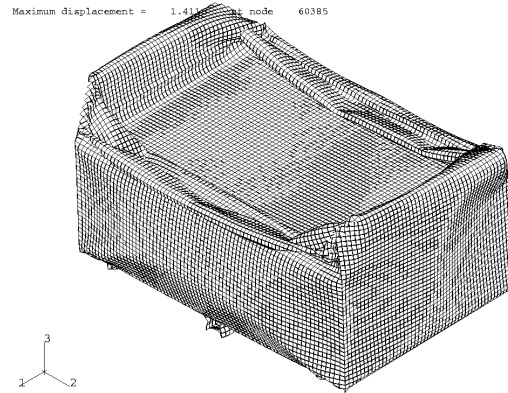


Figure 39. Isometric Top View of the Deformed B-25 Box (Box3) Second from the Top of the Stack modeled with Refined Finite Element Mesh and Calculated with Code-determined Time Increment

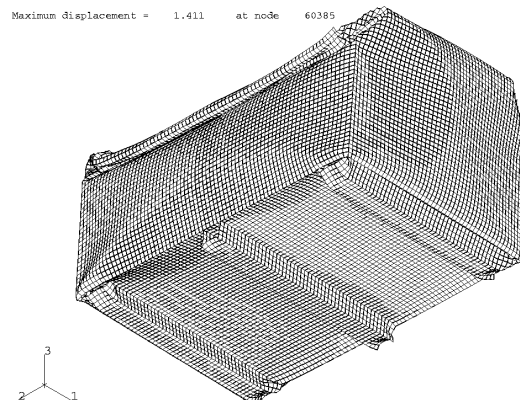


Figure 40. Isometric Bottom View of the Deformed B-25 Box (Box 3) Second from the Top of the Stack modeled with Refined Finite Element Mesh and Calculated with Code-determined Time Increment

The deformed configurations of the two bottom B-25 boxes (Boxes 2 and 1) in the stack are shown in Figures 41, 42, 43 and 44.

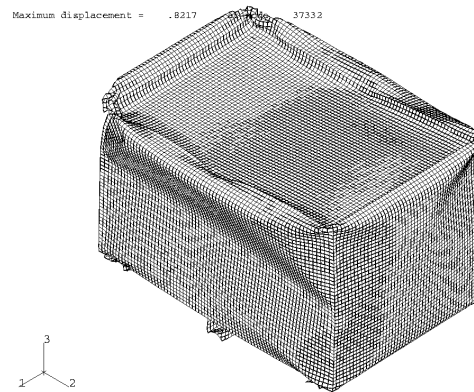


Figure 41. Isometric Top View of the Deformed B-25 Box (Box 2) Second from the Bottom of the Stack modeled with Refined Finite Element Mesh and Calculated with Code-determined Time Increment

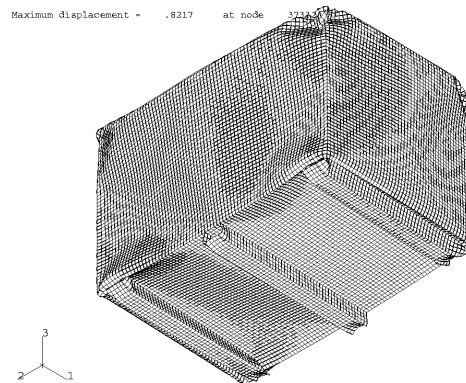


Figure 42. Isometric Bottom View of the Deformed B-25 Box (Box 2) Second from the Bottom of the Stack modeled with Refined Finite Element Mesh and Calculated with Code-determined Time Increment

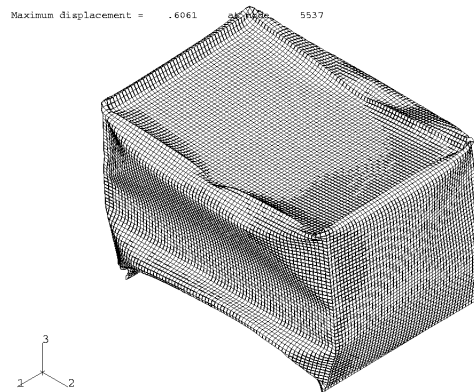


Figure 43. Isometric Top View of the Deformed B-25 Box (Box 1) at the Bottom of the Stack modeled with Refined Finite Element Mesh and Calculated with Code-determined Time Increment

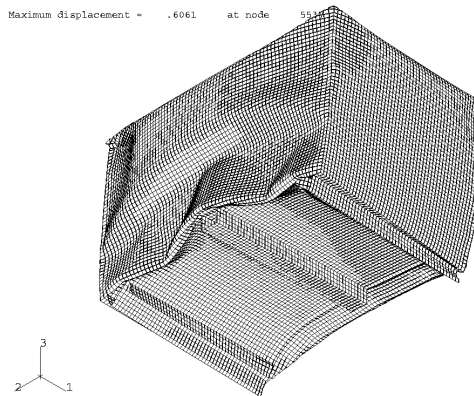


Figure 44. Isometric Bottom View of the Deformed B-25 Box (Box 1) at the Bottom of the Stack modeled with Refined Finite Element Mesh and Calculated with Code-determined Time Increment

The details of the deformed configuration of the B-25 boxes modeled with refined meshes are different from that of the B-25 boxes modeled with coarse meshes. The

deformed configuration of the model with refined meshes exhibits smoother surfaces at corners of sharp deformation than the model with coarse meshes. Nevertheless, the overall characteristics of the deformation configuration of the model with refined meshes and the model with coarse meshes are similar. There may exist an optimal composition (i.e., a combination of the size of finite element mesh, the magnitude of time increment, the precision of the computer and the assigned tolerance for numerical iterations) such that the computational errors in the analysis are minimized. Reduction of the element size by a factor of four is certainly a valid option.

The calculation with the refined model and reduced time increment utilizes much more CPU time (Table 7). The deformed configuration of the refined model with reduced time increment is depicted in Figure 45 (the stack of four B-25 boxes).

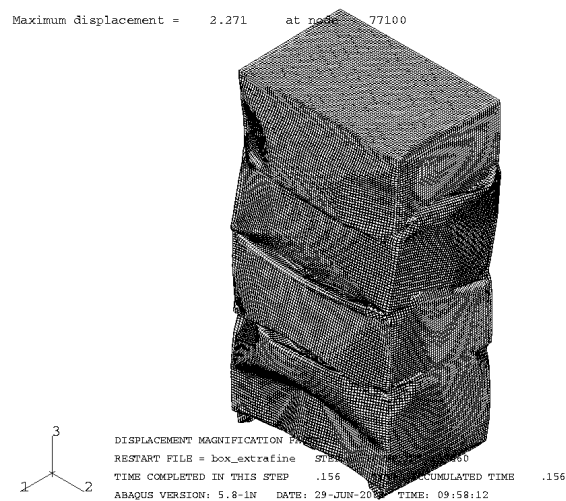


Figure 45. Isometric Top View of the Deformed Stack of Four B-25 Boxes modeled with Refined Finite Element Mesh and Calculated with Fixed Time Increment

The details of the deformed configuration of each individual B-25 box computed with fixed time increment are different from those calculated with the code-determined time increment. Though the patterns of the overall deformation configuration of the B-25 box system computed with finite element meshes of different degrees of fineness and different time increments are characteristically similar. It is essential to show the deformed configuration of each of the B-25 boxes in the stack for future reference and



comparison. The deformed shapes of individual B-25 boxes computed with extra fine mesh and fixed time increment ( $1.0\text{E-}06$  seconds) are depicted in Figures 46 to 53.

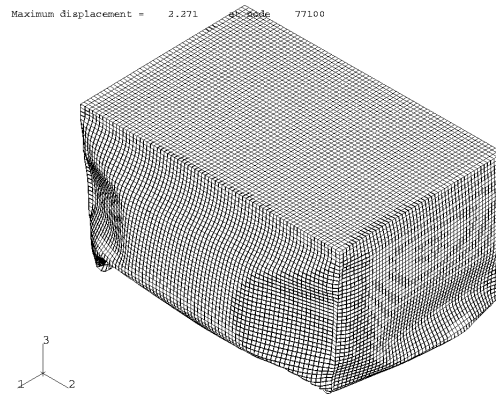


Figure 46. Isometric Top View of the Deformed B-25 Box (Box 4) on the Top of the Stack modeled with Refined Finite Element Mesh and Calculated with Fixed Time Increment

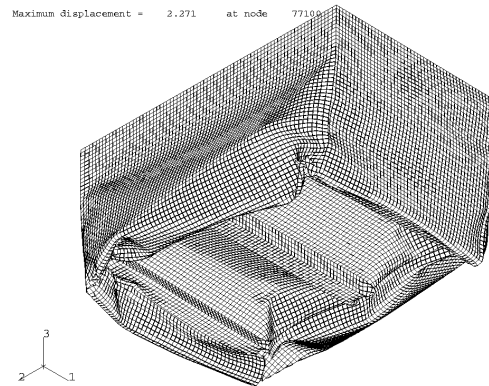


Figure 47. Isometric Bottom View of the Deformed B-25 Box (Box 4) on the Top of the Stack modeled with Refined Finite Element Mesh and Calculated with Fixed Time Increment

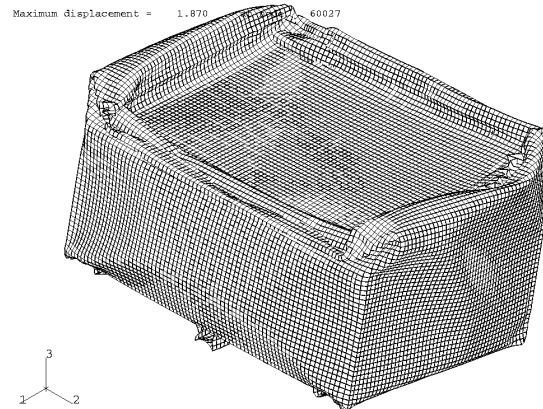


Figure 48. Isometric Top View of the Deformed B-25 Box (Box 3) Second from the Top of the Stack modeled with Refined Finite Element Mesh and Calculated with Fixed Time Increment

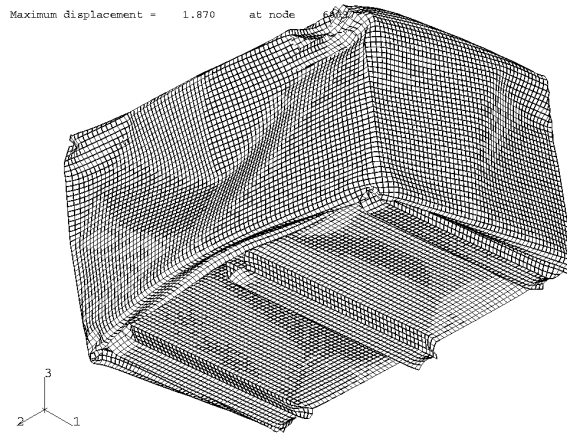


Figure 49. Isometric Bottom View of the Deformed B-25 Box (Box 3) Second from the Top of the Stack modeled with Refined Finite Element Mesh and Calculated with Fixed Time Increment

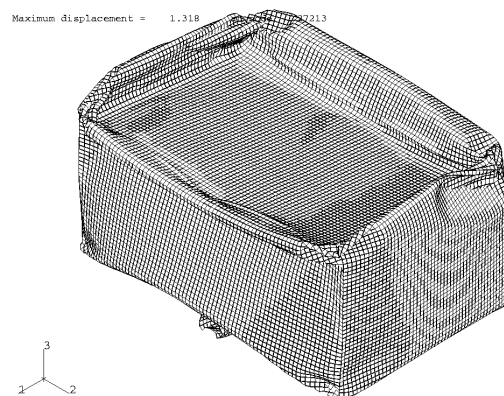


Figure 50. Isometric Top View of the Deformed B-25 Box (Box 2) Second from the Bottom of the Stack modeled with Refined Finite Element Mesh and Calculated with Fixed Time Increment

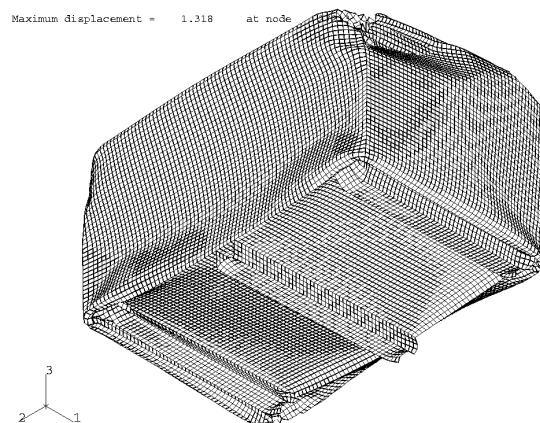


Figure 51. Isometric Bottom View of the Deformed B-25 Box (Box 2) Second from the Bottom of the Stack modeled with Refined Finite Element Mesh and Calculated with Fixed Time Increment

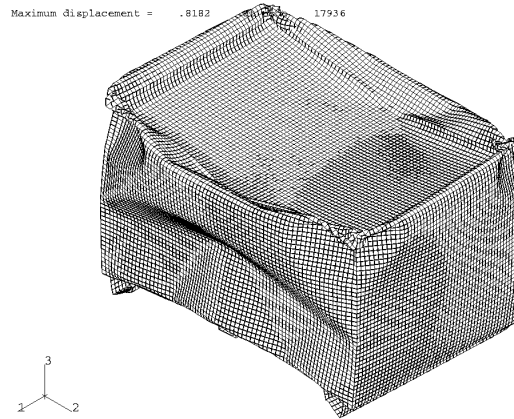


Figure 52. Isometric Top View of the Deformed B-25 Box (Box 1) at the Bottom of the Stack modeled with Refined Finite Element Mesh and Calculated with Fixed Time Increment

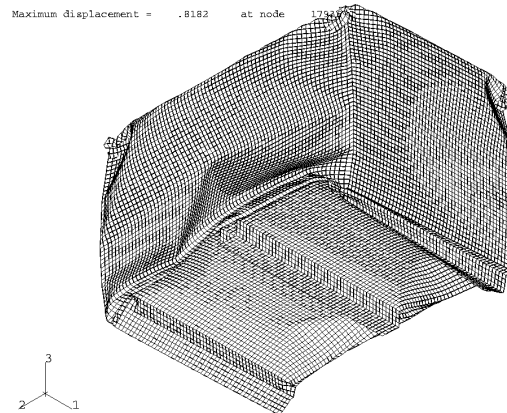


Figure 53. Isometric Bottom View of the Deformed B-25 Box (Box 1) at the Bottom of the Stack modeled with Refined Finite Element Mesh and Calculated with Fixed Time Increment

The deformation configuration of the model with refined meshes provides more details of the dynamic impact. The time history of energies will indicate the true characteristics of the dynamic process. The time history of energies in the whole model with refined mesh is plotted in Figure 54.

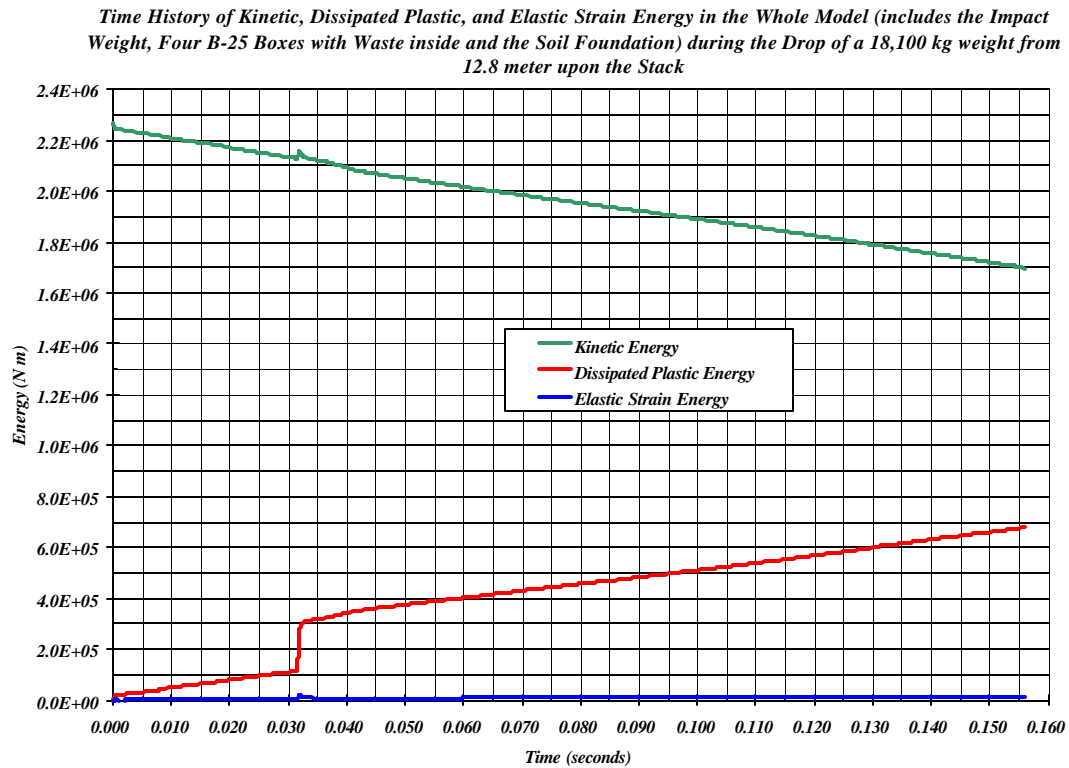


Figure 54. Time History of Kinetic Energy, Dissipated Plastic Energy and Elastic Strain Energy in the Whole Mechanical System Modeled with Refined Mesh

The energy transfer history in the model with refined mesh is, in general, similar to that in the model with coarser mesh (Figure 26). Between the time interval from 0.03 to 0.04 seconds, the three (Kinetic, Plastic and Elastic) energies have an abrupt interchange. Particularly in the model with refined mesh, the sudden jump in the dissipated plastic energy is much more than the reduction of kinetic energy in the system. This sharp plastic energy shift from  $1.1445\text{E}+05$  to  $2.8141\text{E}+05$  N m (up  $1.6696\text{E}+05$  N m) is physically unusual (if not impossible). Certainly a drastic physical incidence in the B-25 box system occurred during this short time interval (from 0.0315 to 0.0320 seconds).

Apparently, the mechanical system reached structural instability at this moment. The refined finite element mesh improves the precision of the geometric configuration of the system during numerical iterations. Consequently the geometric precision enhances the integrity and mechanical strength of the system. The extremely high stress and strain gradients within this short time interval may cause a “bookkeeping error” in the computer code for the energies. In a numerical analysis with explicit integration in time, certain

deformation modes of the elements may induce numerical singularity in the system. During a sudden structural instability (buckling) a large number of elements will deform into singular modes. The conventional “hour-glass” control may fail to work. The slight glitch in kinetic energy at time = 0.032 seconds indicates that a numerical anomaly occurred at this time interval. Since only 314 data points were collected, details of the anomalies in the energy data in the neighborhood of this brief time interval are not clear. The numerical abnormality is isolated and it does not propagate into the rest of calculation. However, once the disturbance got into the dissipated plastic energy record, it is permanent and the glitch will be carried through the entire history. In spite of this isolated numerical singularity, the rest of the calculations are magnificent.

The time history of energies (Figure 55) in the four B-25 boxes may provide some explanation in this mechanical phenomenon.

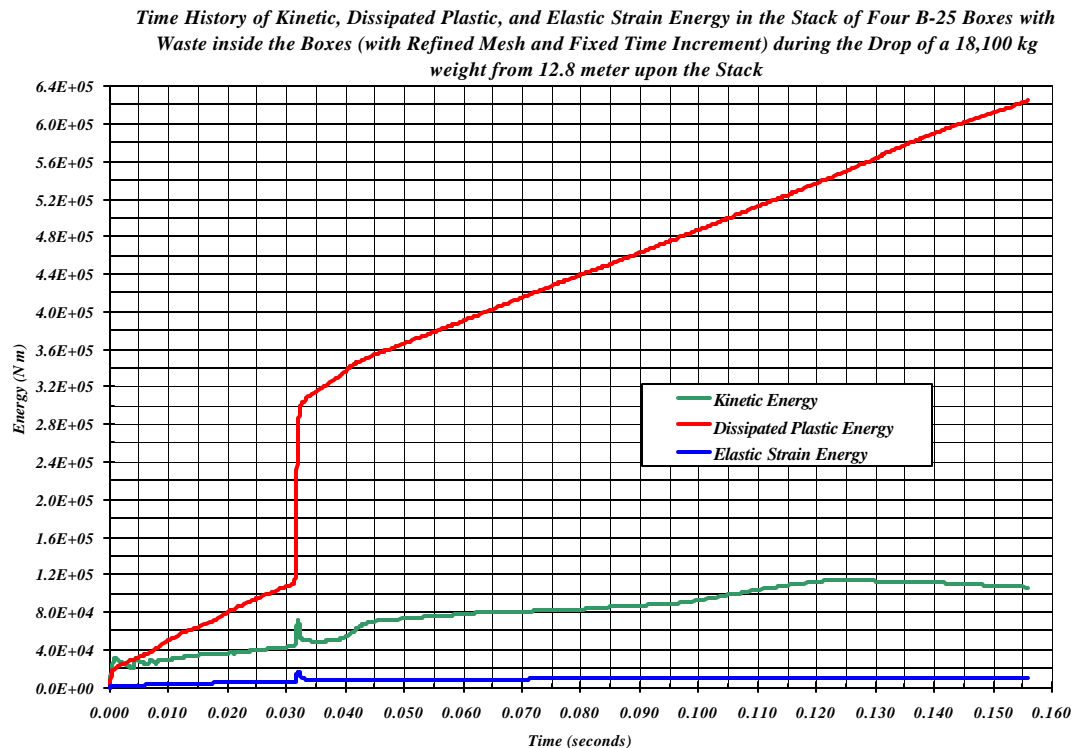


Figure 55. Time History of Kinetic Energy, Dissipated Plastic Energy and Elastic Strain Energy in the Stack of Four B-25 Boxes and Waste inside the Boxes Modeled with Refined Mesh

In the stack of boxes all the three energies show sharp increase in the short time interval. By comparing the time histories of energies of the two calculations, through cross plotting of the curves from both calculations, will enhance understanding of the physical phenomena. Figure 56 shows the time history of the kinetic energy.

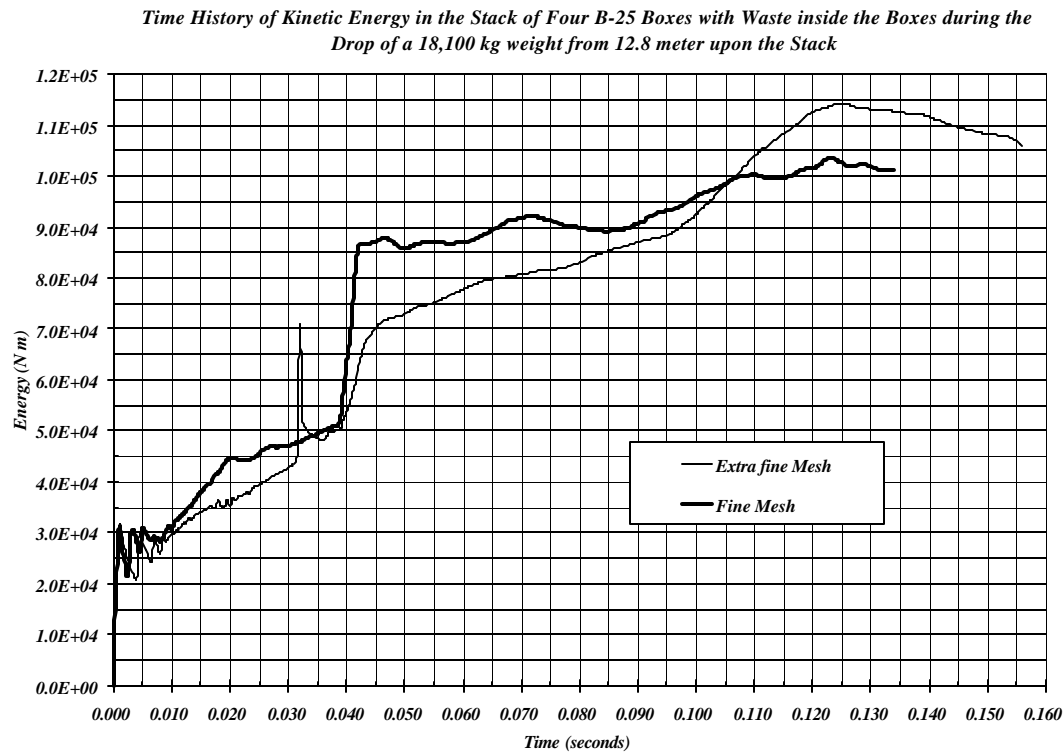


Figure 56. Time History of Kinetic Energy, in the Stack of Four B-25 Boxes and Waste inside the Boxes Modeled with Both Fine and Refined Meshes

Except the spike in the short time interval (0.0315 to 0.0320 seconds) the two curves of the kinetic energy are in good match. The dissipated plastic energy in the model with refined mesh is heavily influenced by the numerical abnormality. A comparison of the two plastic energy curves is shown in Figure 57. The two curves of plastic energy are virtually parallel. The sudden rise of the plastic energy in the model with refined mesh set the two curves apart after the short time interval. The numerical anomaly at time  $\approx 0.032$  seconds is embedded as a permanent part of the dissipated plastic energy. Since the mathematical formulation of the dissipated plastic energy is to collect and accumulate all the unrecoverable energies in the mechanical system. The energy created by the numerical abnormality is a kind of unrecoverable energy and accordingly is saved in the dissipated plastic energy record. Notwithstanding the sudden rise, the two time histories of the dissipated plastic energy are reasonably parallel (Figure 57).

In this mechanical system, the carbon steel that is used for the manufacturing all the B-25 boxes, is the only elasto-plastic material besides the impact weight. In the stack of B-25 boxes, the recoverable strain energy is the elastic strain energy in the carbon steel shell walls. The cross plotting of the elastic strain energies in the stack of boxes during the dynamic compaction computed for the models with different mesh sizes is shown in Figure 58.

The sudden increase of elastic strain energy (at 0.0315 seconds) implies numerical singularity. Of course, mechanical instability (buckling) may also cause sudden rise of elastic strain energy. However, as a precursor to mechanical instability in a system, the rate of increase of elastic strain energy is continuous and smooth, even though it may be a very sharp rise. The elastic strain energy in the analysis with refined mesh indicates rather an abrupt change at 0.0315 seconds and then is gradually relaxed. In the event of mechanical buckling, the elastic strain energy in the system will be built up gradually until it reach the critical value, which is usually the first buckling mode of the system. At the critical loading, the mechanical system will buckle and the elastic strain energy suddenly drops.

In spite of the abrupt change at 0.0315 seconds, the overall elastic strain energy in the calculation with refined mesh is very close to that in the model with fine mesh.

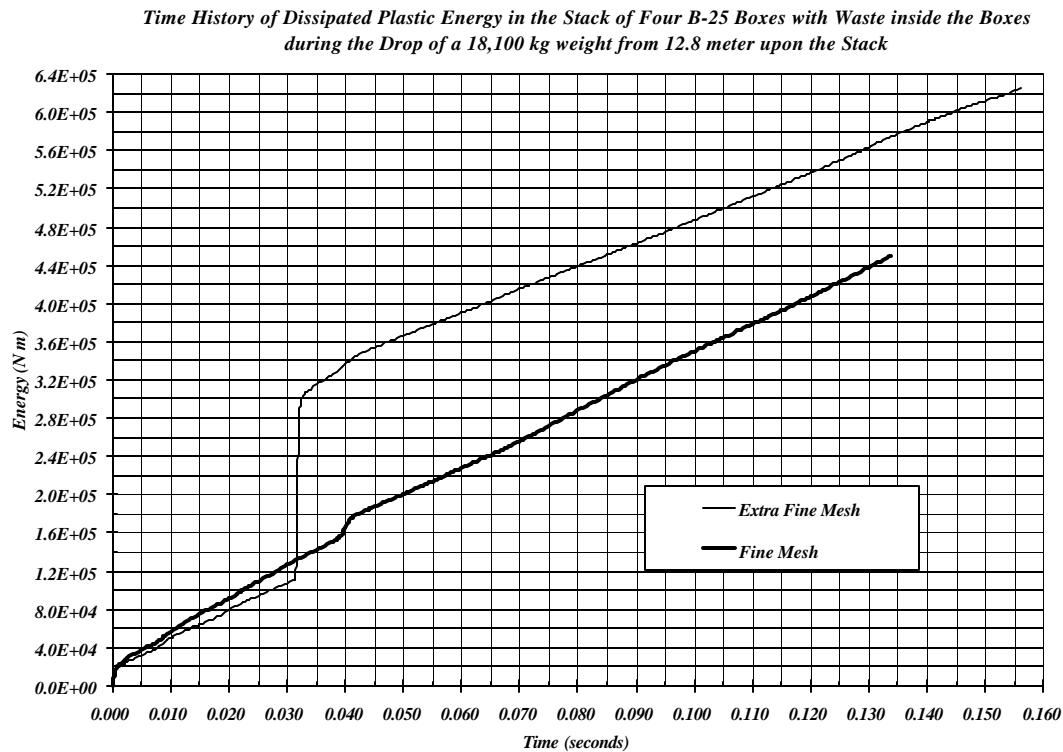


Figure 57. Time History of Dissipated Plastic Energy, in the Stack of Four B-25 Boxes and Waste inside the Boxes Modeled with Both Fine and Refined Meshes



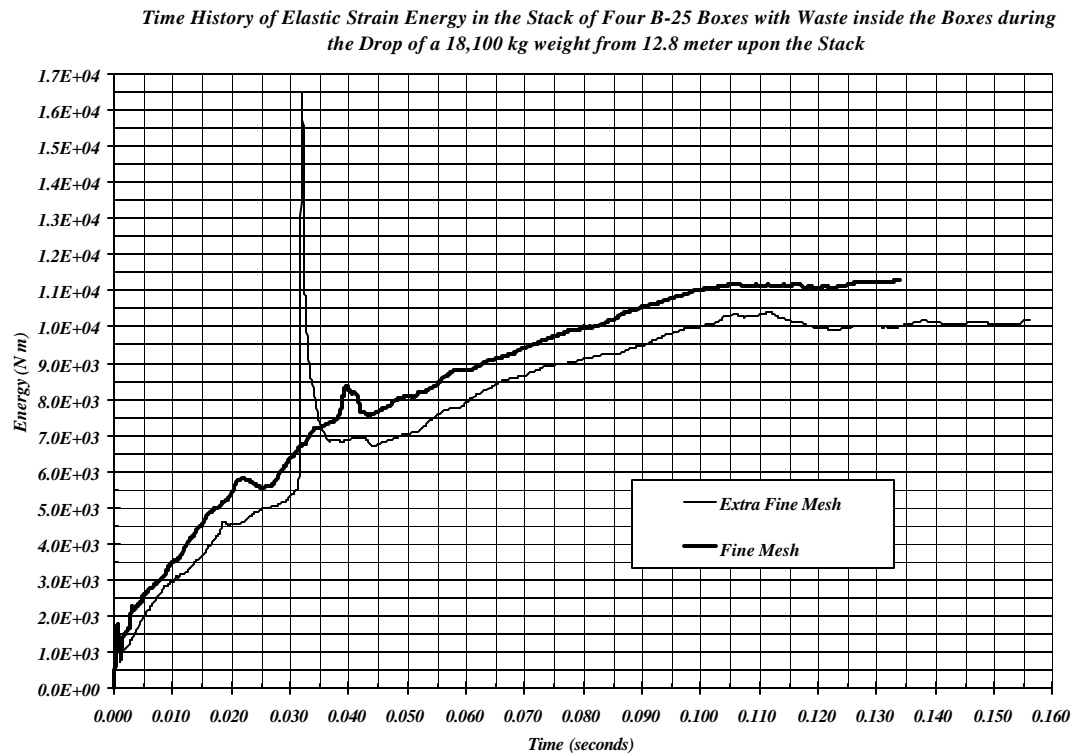


Figure 58. Time History of Elastic Strain Energy, in the Stack of Four B-25 Boxes and Waste inside the Boxes Modeled with Both Fine and Refined Meshes

The model with refined finite element mesh certainly provides more details in the deformation configuration of the B-25 boxes than the model with just fine mesh. However the overall deformation configurations with both meshes are essentially the same. Nevertheless, by comparing the cost in each calculation (Table 7), it indicates that the extravagant CPU time (339,611 seconds) for the refined mesh model may overshadow the benefits resulted from the calculation. Therefore, for this parametric study, the model with fine mesh and fixed time increment is considered sufficient.

## Conclusion

The results of a dynamic compaction analysis are influenced by many physical and computational factors, the major ones are:

- Geometric configuration;
- Kinematic boundary conditions;
- Kinematic initial conditions;
- Mechanical properties of materials;
- Modeling and computational techniques.

Without realistically testing data for the material properties, this analysis utilizes the nominal carbon steel properties for the B-25 boxes. The mechanical properties of soil and waste are practically unknown. In general the mechanical behavior of soil is hydrostatic-pressure dependent and shear sensitive. Therefore the Drucker-Prager Cap model for geological materials is suitable for soil modeling. The material parameters for the model are not available until triaxial soil tests are performed. Whereas for the waste both the material properties and configuration are uncertain. For the super-compacted 55-gallon drummed waste pucks stacked in the boxes, elasto-plastic model is a good choice. For loosely packed paper, cardboard and clothes a constitutive model based on critical state [Schofield, Wroth, 1968] may be selected. The model for crushable foams is one of the critical state models, which has been successfully applied to other crushable materials [Gong, 2000]. The parameters in the model are selected based upon experience and some references. As compared with other mathematical constitutive models, the models for crushable foams and soils are considerably complicated. This analysis shows the flexibility in selecting the most proper constitutive models for each material in the system. With the fundamental models established, the analysis procedure can be applied to mechanical systems that consist of different materials.

The impact weight of 18,100 kg, drops directly upon the top of a stack of four B-25 boxes without the benefit of a layer of soil to absorb the impact and distribute the load. The top of the B-25 box on top of the stack is flatten under the impact load. The dynamic impact transmits through the stack via the propagation of elastic and plastic waves. The mechanical waves reflect back from the soil foundation and refract in the entire structural system.

As the calculation starts, the mathematical model of the stack of boxes is in perfect geometric configuration. The elastic strains are built up in all the metal components. In the thin-walled boxes, the flat plates that are under in-plane compression will eventually become mechanically unstable and buckle. The buckling is usually triggered by geometric imperfection. The truncation errors and other approximations in the numerical computations provide the needed geometric imperfection during the process.

The stack of boxes actually experience at least two major buckling episodes before the calculation is terminated due to excessive strength reduction in the system.

The pseudo-engineering stress-strain curve derived from the calculated results exhibits the episodes of the buckling. The curve also demonstrates the mechanical behaviors of the stack of B-25 boxes. The curve possesses close similarity with the stress-strain curves of cellular solids under dynamic compaction [Gibson, Ashby, 1999]. This similarity implies that the mechanical behaviors of the stack of B-25 boxes under dynamic compaction are essentially comprised of a series of local buckling activities.

Since the boxes are not mechanically connected, no tensile stress exists between the boxes. The mechanical behaviors of the stack of boxes are not completely similar to that of the cellular solids. The deformation configurations of the boxes obtained from this

analysis are very similar to those observed in the dynamic compaction tests [McMullin, Dendler, 1994]

This preliminary finite element analysis serves as an initial parametric study in all aspects of the modeling technique. Besides the geometric and material modeling of the whole mechanical system, the finite element mesh size is also an important factor in achieving accurate solutions.

Within limited computational facilities at SRS, a few different finite element mesh sizes are tested. The first trial mesh did not provide sufficient flexibility in the model. The calculation terminated pre-maturely, which is not included in this report. The second finite element mesh was constructed by quadrupling the number of shell elements in the B-25 boxes. The results are greatly improved. The third attempt intended to prove the credence in finite element analysis that as the mesh size of the model decreases the results from the calculation of the problem will approach the exact solution. This claim is valid only in theory. Because as the finite element mesh is progressively refined, the number of computational operations will be exponentially increased. If the precision of the computer could not be improved accordingly, the truncation errors and other approximations inherited in the finite element analysis formulation (for instance, the explicit integration technique adopted in dynamic analysis) would deprive the quality of the solution.

Further dividing each of the shell elements in the second model into four elements created the finite element mesh of the third refined model. The deformation configurations of the boxes in the refined model provide more details in the heavily deformed corners. Even though, an abnormality showed up in the time history plots of the energies, the rest of the results are still valid.

Besides the fineness of the finite element mesh, the time increment in each step of calculation also influences the accuracy of the results. Fixed time increment is assigned for the fine mesh (second) model. Whereas both code-determined and fixed time increments are used for the refined mesh (third) model. Apparently, the calculation with smaller fixed time increment results in better solution. However the size of the time increment is a function of the element size as well as the material properties. Excessive in reduction of the size of the time increment for integration will produce erroneous results.

The last three calculations are recorded in this report, namely,

- a. The (second) model with fine mesh and fixed time increment,
- b. The (third) model with refined mesh and code-determined time increment,
- c. The (third) model with refined mesh and fixed time increment.

By comparing the final results and the CPU time (Table 7) used in each calculation, the choice is obvious. The second model with fine mesh and fixed time increment will be adopted for further parametric studies in this project.

In the literature most finite element analyses for massive soil structures are carried out only in one- or two-dimensional approximations. The analysis in this report demonstrates the possibility of performing three-dimensional calculations for single stack of B-25 boxes as well as for the engineered trench.

The constitutive models for B-25 boxes, soil foundation and waste are so flexible and versatile. By choosing the appropriate parameters according to testing data, the three models are capable to simulate almost all the mechanical behaviors in the engineered trench system.

The three-dimensional finite element model established in this analysis will be used for further parametric studies. The effects of material corrosion, different waste storage in the B-25 boxes, pre-conditioning of the soil covering and foundation and other physical and geometrical configurations can be realistically simulated.

With the dynamic and static mechanical behaviors of various stacks of B-25 boxes simulated, the equivalent constitutive equations of the stacks of boxes can be used for the engineered trench analysis.

The mechanical properties of the soil foundation are definitely inhomogeneous and nonuniform. The corrosion distribution in the hundreds of B-25 boxes is completely random. Even the configuration, material properties and the void space in each of the hundreds B-25 boxes are not determined. A full stochastic analysis is computationally and financially infeasible.

Therefore with the geometrical and constitutive models constructed in this analysis, a plan for extensive parametric studies should be developed. Comprehensive understanding of the mechanical behaviors of each component in the trench system is necessary for the accurate evaluation of the overall long-term behavior of the engineered trench.

## References

ASM, 1961, “*Metals Handbook*”, eighth edition, volume 1, Properties and Selection: Irons, Steels, and High-Performance Alloy, ASM International Handbook Committee, Materials Park, Ohio 44073.

ASM, 1990, “*Metals Handbook*”, tenth edition, volume 1, Properties and Selection: Irons, Steels, and High-Performance Alloy, ASM International Handbook Committee, Materials Park, Ohio 44073.

Butcher, B. T., Wilhite, E. L., and Phifer, M. A., (SRTC), and Thomas, L. C., and Goldston, W. T. (SWD), 2000, “Program Plan for Evaluating Trench Disposal of Uncompacted Job Control Waste”, SRT-WED-2000-00044, Rev. 0, December 4, 2000. Wilhite, E. L., 2000, “Evaluation of Proposed New LLW Disposal Activity Disposal of LLW in a Mega Trench rather than in Slit Trenches”, WSRC-RP-2000-00217, May 4, 2000.

Dames & Moore, 1987, “Subsidence Study B-25 Metal Containers, Mixed Waste Management Facility”, Report (DMSRP-97) from Charles T. Allen (Partner at Dames & Moore, 455 East Paces Ferry Road, Suite 200, Atlanta, Georgia, 30363) to Alex Guanlao of E. I. Du Pont Nemours & Company, Inc., Savannah River Plant, March 4, 1987

Gibson, L. J., Ashby, M. F., 1999, “*Cellular Solids, Structure and Properties*”, second edition, Cambridge University Press.

Gong, C., 1993, “*Structural Analysis of Closure Cap Barriers, A Pre-test Study for the Bentonite Mat Demonstration Project (U)*”, Technical Report, WSRC-TR-93-508, Task 93-040-0.

Gong, C., 1999a, “*Validation of ABAQUS Finite Element Software for Structural Analysis at the Savannah River Site*”, WSRC/SRTC, Engineering Development Section, G-VVR-G-00007, Rev.1, May 1999.

Gong, C., 1999b, “Spallation Impact Analysis of Plutonium Storage Container at K-area”, WSRC/SRTC, Calculation Note, M-CLC-K-00636.

Gong, C., 2000, “Computational Parametric Analysis of Mechanical Behaviors of Celotex Implanted with Glue Plates,” WSRC/SRTC, Calculation Note, M-CLC-F-00689.

Hill, R., 1950, “*The Mathematical Theory of Plasticity*”, Oxford University Press, Clarendon Press, New York, Oxford.

HKS, 1998, ABAQUS Theory manual, ABAQUS / Explicit User’s Manual, version 5.8-1N, Hibbitt, Karlsson & Sorensen, Inc., 1080 Main Street, Pawtucket, RI 02860-4847, Telephone: 401-727-4200.

Hughes, T. J. R., 1987, "*The Finite Element Method*", Prentice-Hall, Inc., Englewood Cliffs, New Jersey 07632, 1987.

Jones, W. E., Gong, C., Dunn, K. A., 2001, "Scoping Study Plan: Long-term Waste Stabilization Design for Long-term Cover Systems", TTP SR11SS29, SRT-EST-2001-0000105, January 2001.

Malvern, L. E., 1969, "Introduction to the Mechanics of a Continuous Medium", Prentice-Hall, Inc., Englewood Cliffs, New Jersey.

McMullin, S. R., 1994, "Evaluation of Dynamic Compaction of Low Level Waste Burial Trenches Containing B-25 Boxes", WSRC-RP-94-737, September 1994.

McMullin, S. R., Dendler, S. A., 1994, "Dynamic Compaction Facility Test Report (U)", WSRC-TR-94-0159, Rev. 1, Environmental Restoration Department, March 1994.

MSC, 1999, MSC / PATRAN, version 8.5, The MacNeal-Schwendler Corporation, 815 Colorado Boulevard, Los Angeles, Telephone: 213-258-9111.

Phifer, M. A., Serrato, M. G., 2000, "Preliminary E-area Trench Subsidence Evaluation", Inter-Office Memorandum to L. C. Thomas, SRT-EST-2000-00105, January 18, 2000.

Phifer, M. A., 2000, "Technical Task Plan (TTP): Long-term Waste Stabilization Design for Long-term Cover Systems", SR1-1-SS-99, March 28, 2000.

Phifer, M. A., 2000, "Technical Task Plan (TTP): Long-term Waste Stabilization Design for Long-term Cover Systems", SR1-1-SS-29, July 24, 2000.

Press, W. H., Flannery, B. P., Teukolsky, S. A., and Vetterling, W. T., 1986, "*Numerical Recipes, The Art of Scientific Computing*," Cambridge University Press, Cambridge, London, New York.

Procurement Specification, 2000, "Low Level Waste B-12 & B-25 Box (U)", Specification No. C-SPP-G-00101, Revision 4, WSRC, July 26, 2000.

Schofield, A. and Wroth, C. P., 1968, "Critical State Soil Mechanics", McGraw-Hill, New York.

Timoshenko, S. P., Gere, J. M., 1961, "*Theory of Elastic Stability*," Second Edition, McGraw-Hill Book Company, Inc., New York, 1961

Timoshenko, S. P., Woinowsky-Krieger, S., 1959, "*Theory of Plates and Shells*," Second Edition, McGraw-Hill Book Company, Inc., New York, 1959

**DISTRIBUTION**

AYLWARD, ROBERT S. (1)	773-42A (ROOM 281)
BUTCHER, BYRON T., JR. (1)	773-43A (ROOM 216)
DIVECCHIA, LINDA-LEE F.(1)	773-42A (ROOM 144)
DUNN, KERRY A. (1)	773-41A (ROOM 182)
DWYER, STEPHEN F. (1)	Sandia National Laboratories P. O. Box 5800, MS-0919 Albuquerque, NM 87185-0719
FAYER, MICHAEL J. (1)	Pacific Northwest National Laboratory Environmental Technology Division Mail Stop K9-33 Battelle Boulevard, P. O. Box 999 Richland, WA 99352
GOLDSTON, WELFORD T. (1)	705-3C (ROOM 105)
HARRIS, MARY K. (1)	773-42A (ROOM 219)
HOLDING-SMITH, CYNTHIA P. (1)	773-42A (ROOM 146)
HUDSON, PETER IAN (1)	705-3C (ROOM 126)
JONES, WILLIAM ELDON (12)	773-42A (ROOM 260)
MCMULLIN, SCOTT R. (1)	703-A (ROOM E118S)
PHIFER, MARK A. (1)	773-42A (ROOM 252)
Scientific & Technical Information (4)	703-43A
SERRATO, MICHAEL G. (5)	773-42A (ROOM 217)
THOMAS, LLOYD C. (1)	705-3C (ROOM 116)
TREGER, THOMAS M. (1)	703-A (ROOM B202)
WACH, STEVEN T. (1)	773-42A (ROOM 143)
WILHITE, ELMER L. (1)	773-43A (ROOM 214)